Mitochondrial One-Carbon Flux has a Growth-Independent Role in Promoting Breast Cancer Metastasis

Nicole Kiweler[1], Catherine Delbrouck[1,2], Laura Neises[1], Vitaly I. Pozdeev[3], Leticia Soriano-Baguet[2,4,5], Feng Xian[6], Mohaned Benzarti[1,2], Lara Haase[1,2,5], Maryse Schmoetten[3], Christian Jaeger[5], Muhammad Zaeem Noman[1], Alexei Vazquez[7], Bassam Janji[1], Gunnar Dittmar[2,6], Dirk Brenner[4,5,8], Elisabeth Letellier[3], Johannes Meiser[1*]

[1]Department of Oncology, Luxembourg Institute of Health, Luxembourg, Luxembourg

[2]Faculty of Science, Technology and Medicine, University of Luxembourg, 2 avenue de Université, Esch-sur-Alzette, Luxembourg

[3]Faculty of Science, Technology and Medicine, Department of Life Sciences and Medicine, Molecular Disease Mechanisms Group, University of Luxembourg, Esch-sur-Alzette, Luxembourg

[4]Experimental & Molecular Immunology, Department of Infection and Immunity, Luxembourg Institute of Health, Luxembourg, Luxembourg

[5]Luxembourg Centre for Systems Biomedicine, University of Luxembourg, Esch-sur-Alzette, Luxembourg

[6]Proteomics of Cellular Signaling, Quantitative Biology Unit, Luxembourg Institute of Health, Luxembourg, Luxembourg

[7]Institute of Cancer Sciences, University of Glasgow, Glasgow, United Kingdom

[8]Odense Research Center for Anaphylaxis, Department of Dermatology and Allergy Center, Odense University Hospital, University of Southern Denmark, Odense, Denmark

[*]Correspondence:

Email: johannes.meiser@lih.lu

Twitter: @JohannesMeiser

Graphical Abstract

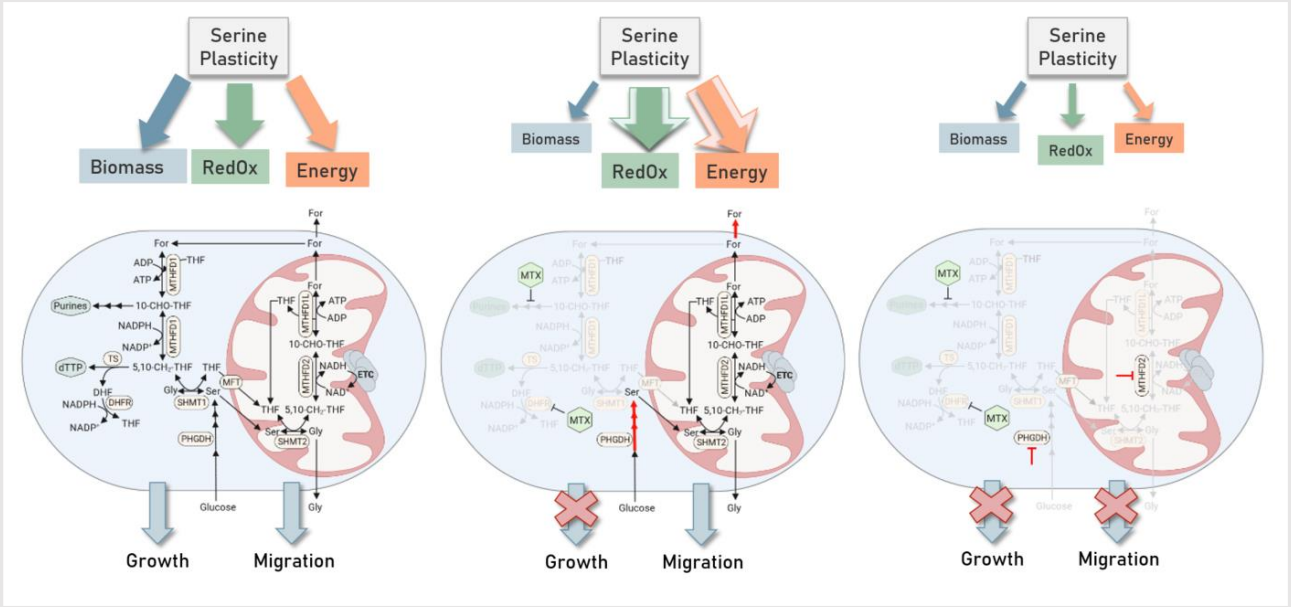

Abstract

Progression of primary cancer to metastatic disease is the most common cause of death in cancer patients with minimal treatment options available. Canonical drugs target mainly the proliferative capacity of cancer cells, which often leaves slow-proliferating, persistent cancer cells unaffected. Thus, we aimed to identify metabolic determinants that enable cell plasticity and foster treatment resistance and tumor escape.

Using a panel of anti-cancer drugs, we uncovered that antifolates, despite their strong growth arrest function, do not at all reduce the cancer cell's motility potential, indicating that nucleotide synthesis is dispensable for cell motility. Prolonged treatment even selected for more motile cancer subpopulations. We found that cytosolic inhibition of DHFR by MTX only abrogates cytosolic folate cycle, while mitochondrial one-carbon cycle is still highly active. Despite a decreased cellular demand for biomass production, *de novo* serine synthesis and formate overflow are increased, which suggests that mitochondria provide a protective environment that allows serine catabolism to support cellular motility during nucleotide synthesis inhibition.

Enhanced motility of growth-arrested cells was reduced by inhibition of PHGDH-dependent serine *de novo* synthesis and genetic silencing of mitochondrial one-carbon cycle. *In vivo* targeting of mitochondrial one-carbon cycle and formate overflow strongly and significantly reduced lung metastasis formation in an orthotopic breast cancer model. In summary, we identified mitochondrial serine catabolism as a targetable, growth-independent metabolic vulnerability to limit metastatic progression.

Keywords

One-Carbon Metabolism, Formate Overflow, Cancer Metastasis, Metabolism, Serine, Migration, Antifolate, Methotrexate

Introduction

Many primary tumors can be targeted by specific treatment schemes. Thus survival rates of patients harboring primary tumors steadily increases. However, in case of tumor relapse and metastasis formation, effective therapies are mostly lacking with the consequence that secondary tumors account for the majority of cancer deaths [1].

Classical chemotherapeutic approaches to counteract cancer growth aim to target biomass production by interfering with the synthesis of proteins, lipids, and nucleotides and thereby directly interfere with central pathways of cancer cell metabolism. Consequently, it is well studied that beneficial metabolic reprogramming is fundamental for cancer cells to maximize the synthesis of essential lipids, proteins and nucleotides in order to drive the excessive growth rates observed within the primary tumor and the secondary metastasis [2, 3].

However, changes in cancer cell metabolism during stages of reduced biomass production, for example upon chemotherapy or when cancer cells transition along the metastatic cascade, are far less well described [3]. Targeting metabolic cues to not only reduce cancer growth but also to metabolically interfere with invasive and migratory properties of cancer cells represents a desirable therapeutic approach to ultimately prevent metastatic progression of the initial disease. We have previously shown that a reduction of biomass demand can result in the increased formate release from cancer cells to their surrounding microenvironment [4]. The mechanistic basis for such a formate overflow phenomenon especially in growth inhibited cancer cells, is the rate of serine catabolism through serine one-carbon cycle (SOC).

Within this metabolic pathway, that spans between cytosol and mitochondrion [5], extracellular and *de novo* synthesized serine is catabolized to support all three essential pillars of metabolism: biomass production, redox equivalent and bioenergy generation [6]. Especially metastasizing cancer cells need to selectively and dynamically adopt their cellular metabolism to fulfil these three major metabolic constraints along every step of the metastatic cascade [3, 7]. For example, metabolic rewiring during the growth-independent process of tumor cell escape and dissemination is dominated by bioenergetic and redox demands rather than biosynthetic needs [3, 7, 8]. Importantly, serine plasticity allows to readjust the metabolic outputs of serine catabolism through SOC towards either of the three metabolic hallmarks [6]. For example, upon high growth rates, serine, glycine and formate production from SOC is required to support the synthesis of anabolic building blocks such as proteins, lipids, heme, glutathione, and nucleotides. In contrast, upon energy limitation, most of serine derived carbon is excreted in the form of formate or CO_2 and SOC is maximized towards energy production in form of NADH and ATP [4]. Alternatively, upon oxidative stress, the demand for glycine to support GSH synthesis is superior [9]. Previously, we could show that the rate of serine catabolism to formate is significantly increased in adenomas of the small intestine and breast tumors compared to normal tissue and, that increased formate levels can increase the invasiveness of cancer cells [10]. In addition, other labs also reported a role of serine metabolism in the context of metastasis [11-13]. However, the focus of these recent works is mainly set on the relevance of serine *de novo* synthesis via phosphoglycerate dehydrogenase (PHGDH) itself instead of addressing the subsequent catabolism of serine via SOC for metastatic progression. Available mechanistic studies on the role of SOC in context of metastasis were carried out mainly with a focus on the proliferative capacities essential for metastatic outgrowth [11, 12, 14] rather than analyzing metabolic requirements that support the growth-independent metastatic processes of dissemination. In the absence of such growth demands and under certain metabolic stress conditions, we have previously demonstrated that cells increase

their rate of formate overflow via SOC [4, 10], which further manifests that regulation of SOC represents a metabolic switch of key interest especially in, but not limited to, the growth-independent stages of metastatic outgrowth.

In the present study, our goal was to identify metabolic processes that are specifically important to support cancer cell motility in the growth independent process of metastatic dissemination. We have discovered, that antifolates, while having strong growth arresting properties, do not decrease the cellular motility potential. Using antifolates as a tool compound to separate metabolic processes from growth and motility processes, we have identified SOC as central metabolic pathway that supports the cellular motility potential. Specifically, the mitochondrial SOC is required to support the observed motility, while the cytosolic part, that is essential for proliferation, is dispensable for the cell's motility potential. Finally, we provide evidence that formate overflow via mitochondrial SOC is a targetable growth-independent vulnerability to limit breast cancer metastasis. The identified metabolic vulnerability might have clinical implications for metastatic progression in context of growth-inhibiting chemotherapies.

Results

Inhibition of major anabolic synthesis routes differentially impacts the motility potential of cancer cells

To assess the relative importance of different metabolic pathways for cancer cell migration, we employed a panel of metabolic perturbations targeting glycolysis, mitochondrial oxidative phosphorylation (OxPhos) as well as lipid, protein, and nucleotide synthesis (**Figure 1A**). All metabolic interventions were effectively inhibiting the growth and cell cycle progression of MDA-MB468 breast cancer cells and the chosen drug concentrations had none to mild toxic effects after 48 h treatment (**Figure 1B-C, S1A**). Inhibition of glycolysis, OxPhos, lipid, and protein synthesis significantly reduced migration of MDA-MB468 cells (**Figure 1D**). Surprisingly and in contrast to all other growth-inhibiting conditions, inhibition of nucleotide synthesis with any of the applied drugs did not diminish migration of MDA-MB468 cells (**Figure 1E**). Calculation of the area under curve (AUC) allowed us to quantitatively compare wound closure upon the diverse metabolic perturbations over time (**Figure 1D, E**) and confirmed that wound closure was significantly reduced upon rotenone (Rot), galactose (Gal), simvastatin (SIM) and sirolimus (rapamycin, SIR) treatment, while treatment with the antifolates methotrexate (MTX) and pemetrexed (PEM), as well as with hydroxyurea (HU) and clofarabine (CLO) did not affect or did even significantly increase wound closure in Scratch assays in comparison to fully proliferative, untreated control cells (**Figure 1D, E**). This divergent effect of nucleotide synthesis inhibition from all other metabolic perturbations becomes further visible, when directly correlating our data on MDA-MB468 cell migration with cell growth in response to treatment (**Figure 1F, G**). While cell migration correlates with reduced cell growth for all other metabolic perturbations, nucleotide synthesis inhibition does not reduce cell migration in correlation to growth inhibition (**Figure 1F, G**). This finding could be verified in LN229 glioblastoma and 4T1 breast cancer cells (**Figure S1B-D**). To further technically confirm this finding, we assessed migration of MDA-MB468 cells in a trans-well assay. Similar to our previous findings, we could show no reduction of cell migration in response to neither MTX nor PEM (**Figure 1H**). Using ECM-collagen coating in trans-well assay, we found that nucleotide synthesis inhibition furthermore had no impact on cancer cell invasion (**Figure 1H**). Trans-well assay findings were confirmed using LN229 and 4T1 cells (**Figure S1E, F**). Given this pro-migratory effect of nucleotide synthesis inhibition in growth-arrested cancer cells, we generated MTX-resistant MDA-MB468 cells

by long-term cultivation in 50 nM MTX for 2 months. The resulting, MTX-resistant MDA-MB468 cells proliferate in the presence of increasing concentrations of MTX and show enhanced migratory capacity when compared to the parental MDA-MB468 cell line (**Figure 1I, J**).

In conclusion, the perturbation of any major anabolic route results in growth repression, its impact on cell migration however highly depends on the targeted metabolic pathway, with nucleotide synthesis being an ineffective target to abrogate cell motility. Considering that cell proliferation contributes to the final migratory outcome, cell migration must in fact be increased upon nucleotide synthesis inhibition to compensate for the reduced growth rate. Different means of metabolic growth repression thus differentially impact cell motility and do not necessarily result in decreased cell migration. Furthermore, prolonged nucleotide synthesis inhibition is even selecting for drug-resistant, motile cancer subpopulations.

MTX treatment triggers a ROS-driven EMT phenotype

One of the most established and extensively described nucleotide synthesis-inhibiting clinical drugs is the dihydrofolate reductase inhibitor MTX. MTX impedes the regeneration of tetrahydrofolate (THF), which is a central enzymatic cofactor during purine and pyrimidine synthesis [15]. As MTX induces the strongest growth repression without impacting cell death (**Figure 1B, C**) and has no effect on cell migration (**Figure 1E**), we selected it as a tool compound to study and identify metabolic processes that are essential to support cell migration and metastasis independent of cell proliferation. We tested multiple MTX concentrations and chose a concentration of 50 nM, which is not only significantly growth- and cell cycle-arresting in MDA-MB468 cells (**Figure 1B, S1A, S2A**), but has also been shown to be within the therapeutic window [16-19]. We observed that 48 h MTX treatment of MDA-MB468 cells resulted in altered cellular morphology with individual cells visibly increasing in cell size (**Figure 2A**). Following treatment, single cells exhibited an outstretched cell shape with protruding edges, indicative of a remodeling of the cellular cytoskeleton (**Figure 2A**). MTX-resistant MDA-MB468 cells showed comparable morphologic alterations (**Figure S2B**). We found that the observed cell cycle and proliferation arrest upon MTX treatment is reversible, as MDA-MB468 cells promptly regained growth properties (**Figure S2C**) and re-established proliferation by restarting cell cycle progression (**Figure S2D**) upon MTX removal. Using [U-^{13}C]serine tracer and metabolic flux analysis, we could confirm that the concentration of 50 nM MTX is sufficient to significantly diminish the flux of labelled serine carbon units via methylenetetrahydrofolate to ATP (**Figure 2B**). Of note, nucleotide synthesis was partially restored in MTX-resistant MDA-MB468 cells (**Figure S2E**). Using stable isotope labeling by amino acids in cell culture (SILAC) and subsequent quantitative proteomics analysis, we could confirm the efficiency of the selected MTX dose as the expression of mechanistic targets of MTX such as dihydrofolate reductase (DHFR), thymidylate synthase (TS), and thymidine kinase (TK) were confirmed to be regulated by treatment as expected (**Figure 2C, S2F**). Interestingly, we also found superoxide dismutase (SOD) to be one of the most significantly upregulated enzymes in response to treatment (**Figure 2C, S2F**), which corresponds to prior reports that depict MTX as a potent inducer of oxidative stress [20-22]. We could confirm these prior findings by measuring a moderate but significant increase of mitochondrial and cytosolic reactive oxidant species (ROS) within MDA-MB468 cells in response to MTX (**Figure 2D, E**). Moreover, the mesenchymal marker protein vimentin (VIM) and transforming growth factor-beta2 (TGFB2) were found to be highly upregulated in the global proteomics approach following MTX treatment (**Figure 2C, S2F**). This finding corresponds to earlier reports, that highlight the potential of oxidative stress as a driver of cancer cell migration and the transformation of cancer cells via

epithelial-mesenchymal transition (EMT) [6, 23-28]. We thus analyzed MDA-MB468 cells for the expression levels of the major regulators of EMT - the transcription factors ZEB1, ZEB2, SNAIL, and SLUG – and found ZEB1 and ZEB2 expression as well as VIM expression to be upregulated over time in response to MTX treatment (**Figure 2F**). Similar upregulation of ZEB1, ZEB2, and VIM expression was observed in the MTX-resistant MDA-MB468 cell line when compared to the parental MDA-MB468 cell line (**Figure 2G**). We could confirm this upregulation of the expression of VIM mRNA and protein level following MTX-treatment as well as in the MTX-resistant MDA-MB468 cell line by Western Blot (**Figure 2H, I**). MTX-treatment did also induce the expression of the collagenase MMP9 (**Figure 2J**), an enzyme which is involved in the degradation of the extracellular matrix during cancer cell migration [29]. To investigate the relevance of ROS as a potential trigger for this observed EMT phenotype in response to MTX treatment, we employed N-acetylcysteine (NAC) as an antioxidant and were able to reduce ROS levels in MTX-treated MDA-MB468 cells (**Figure 2K**). While NAC alone already reduced the cell migration, combined treatment with NAC and MTX resulted in a significant reduction of MTX-induced cell migration (**Figure 2L**). Correspondingly, NAC treatment also prevented the EMT phenotype induction in MTX-treated MDA-MB468 cells with the exception of ZEB1 (**Figure 2M**). These findings indicate that ROS induction upon MTX promotes EMT and sustains migration. In conclusion, the moderate increase in cellular ROS levels after MTX acts as a pro-migratory stimulus that subsequently results in the establishment and long-term selection of phenotypically altered cancer cell subpopulations. However, research in the past has raised awareness, that antioxidant treatment is not a promising cancer treatment strategy with mixed, and not always beneficial, outcomes in clinical trials [30, 31]. Therefore, our aim was to further investigate the metabolic mechanisms that support enhanced cell migration in the presence of the nucleotide synthesis and growth-inhibiting tool compound MTX.

MTX-treated cells sustain high metabolic rates and enhance *de novo* serine synthesis

Having established that growth arrested MDA-MB468 cells maintain full migratory and invasive properties under MTX treatment, we wanted to define metabolic mechanisms that maintain this pro-invasive EMT phenotype. To that end, we focused on central carbon metabolism using [U-^{13}C]glutamine and [U-^{13}C]glucose to monitor glycolytic activity and glucose- or glutamine-derived carbon oxidation through the TCA cycle (**Figure 3A, D**). Absolute uptake rates of glutamine and glutamate were sustained in response to MTX treatment (**Figure 3B**), while the relative flux of [U-^{13}C]glutamine throughout the TCA-cycle was significantly increased in response to MTX (**Figure 3C**). Absolute quantification of uptake and release rates of glucose and lactate also revealed sustained high glycolytic rates upon MTX treatment (**Figure 3E**). This came as a surprise, as lactate release rates were previously shown to generally correlate with cell growth rates [32]. Here however, MTX-treated and growth-arrested cells maintained their glycolytic rate and associated lactate release rates at constant high levels. This indicates a constant generation of glycolysis-derived ATP even in the presence of reduced energetic demand for anabolic reactions under growth-arresting conditions. Consequently, [U-^{13}C]glucose distribution within the TCA-cycle was comparable in untreated and MTX-treated MDA-MB468 cells (**Figure 3F**) as well as in 4T1 and LN229 cells (**Figure S3A, B**). It has previously been shown that MTX inhibits OCR in HCT116 cells [33]. We could replicate this finding and observed a ~ 30 % reduction in OCR in HCT116 cells upon MTX (**Figure S3C**). However, OCR in MDA-MB468, LN229, and 4T1 cells was sustained at control level in response to MTX (**Figure 3G**), which indicates cell line specific effects of MTX on OCR. Overall, these findings indicate that, despite decreased growth rates, central carbon metabolism and mitochondrial

respiration are sustained in response to MTX treatment, with an additional increased oxidative glutamine metabolism. Furthermore, we observed that MTX treatment significantly increased the relative flux of glucose to serine via the serine *de novo* synthesis pathway despite decreased anabolic demands for nucleotide synthesis (**Figure 3H, S3D**). The serine *de novo* synthesis pathway is catalyzed by three enzymes - PHGDH, PSPH, and PSAT1, whose protein levels remained unchanged in response to MTX treatment in MDA-MB468, MDA-MB231, 4T1 and LN229 cells (**Figure S3E-H**). In agreement with Diehl et al. [34], who showed that changes in NAD^+/NADH ratio can increase PHGDH activity and in consequence serine *de novo* synthesis rates, we observed an increased NAD^+/NADH ratio upon MTX (**Figure 3I**). Congruently, yet somewhat surprisingly, MTX treatment did also increase the proportion of labeled, extracellular formate derived from [U-^{13}C]glucose through serine and the mitochondrial SOC (**Figure 3J**). This might indicate that the mitochondrial part of the SOC is not as inhibited by MTX treatment as its cytosolic part. In summary, we demonstrate that, despite decreased metabolic demand for biomass production, MTX-treated cells sustain high metabolic rates comparable to fully proliferating cells. Additionally, treated cells exhibit increased rates of serine synthesis and formate excretion.

Mitochondria protect SOC-dependent serine catabolism in the presence of MTX

Given our finding of increased formate labeling derived from [U-^{13}C]glucose (**Figure 3J**), we hypothesized that the influence of MTX-mediated DHFR inhibition on mitochondrial SOC is, in contrast to cytosolic SOC, limited (**Figure 4A**). To test this hypothesis, we employed [U-^{13}C]serine tracing to further characterize serine flux through SOC. We observed that despite inducing growth-arrest, MTX did not alter the rates of serine consumption and glycine release neither in MDA-MB468 nor in LN229 cells (**Figure 4B, S4A**). This is a remarkable observation for two reasons: (i) as the major route of serine catabolism is via SOC [4], one would have expected that MTX-mediated inhibition of DHFR decreases cellular serine consumption; (ii) as cell dry mass composition is constituted by around 60 % of proteins [35], growth arresting conditions upon MTX should result in decreased consumption rates of proteinogenic amino acids. In fact, a general trend for decreased consumption of other essential amino acids could be observed (**Figure S4B**) in response to MTX. Most strikingly, the total release rate of formate as well as of labeled M+1 formate derived from [U^{13}C]serine into the culture medium was significantly increased (**Figure 4C**) in MDA-MB468 cells and sustained in LN229 cells (**Figure S4C**). We could confirm using Plasmax medium [36] that sustained serine and glycine consumption and release (CORE) rates and increased formate overflow via SOC in the presence of MTX can be recapitulated in a culture medium closer to the physiological state of human physiology (**Figure S4D**). SOC follows a cycle in which serine can be resynthesized in the cytoplasm and mitochondrion from glycine via serine hydroxymethyltransferase 1 and 2 (SHMT1, SHMT2) (**Figure 4A**). As the mitochondrial SHMT2 reaction is highly reversible, the serine labeling pattern from [U^{13}C]serine is composed of a mix of fully labeled M+3 isotopologues as well as M+1 and M+2 isotopologues, which represent the different recombination events with labeled and unlabeled glycine [4, 5, 37]. Consequently, M+1 and M+2 serine isotopologues are expected to be absent upon complete SOC inhibition. Intriguingly, DHFR inhibition with MTX neither completely abrogated serine M+1 and M+2 isotopologues upon [U-^{13}C]serine nor did it affect the serine to glycine ratio in MDA-MB468 or LN229 cells (**Figure 4D, E, S4E, F**)**.** This observation of diminished, but not abolished serine M+1 and M+2 isotopologues indicates a sole inhibition of cytosolic but not mitochondrial SOC under MTX treatment. To comparatively demonstrate how sole or dual inhibition of cytosolic and mitochondrial SOC affects serine

MID, we analyzed a panel of CRISPR generated knockouts in HAP1 cells in which either the cytosolic (SHMT1), the mitochondrial (MFT, SHMT2), or both compartments (FPGS, MFT+SHMT1) of SOC were abrogated [38]. In accordance with our findings and resulting conclusion that MTX solely abolishes cytosolic SOC, cytosolic SHMT1 KO did not eliminate intermediary M+1 and M+2 serine isotoplogues from [U-^{13}C]serine, whereas mitochondrial or combined cytosolic and mitochondrial inhibition of SOC upon MFT KO, SHMT2 KO, FPGS KO and MFT+SHMT1 KO resulted in a complete loss of M+1 and M+2 serine isotopologues (**Figure 4F**). SHMT1 KO reduced serine M+1 and M+2 isotopologue abundance comparable to MTX treatment (**Figure 4F**). In mutants harboring a full inhibition of SOC or mitochondrial SOC, we additionally observed an increase of the serine to glycine ratio, whereas MTX treatment and SHMT1 KO slightly reduced serine to glycine ratio (**Figure 4G**). Overall, these results indicate that the mitochondrion provides a protected cellular environment that permits serine catabolism with formate overflow via SOC even in the presence of the antifolate MTX.

Targeting of serine *de novo* synthesis decreases MTX-dependent cancer cell migration

Having confirmed increased serine synthesis from glucose and subsequent formate overflow through mitochondrial SOC in response to MTX treatment, we set out to determine if interfering with this metabolic pathway is a mean to counteract enhanced cell migration upon MTX. To identify a suitable inhibitor of serine *de novo* synthesis, we tested multiple available allosteric and one competitive inhibitor of PHGDH. We found that the competitive inhibitor BI-4916 (BI) had superior efficiency when compared to different allosteric inhibitors such as WQ-2101 (WQ), NCT-502 (NCT), and CBR-5884 (CBR) as can be seen in the isotopic labelling pattern of serine from [U-^{13}C]glucose tracer (**Figure 5A**). Isotopic labelling of released formate from [U-^{13}C]glucose tracer was also profoundly diminished after BI treatment alone or in combination with MTX (**Figure 5B**). Additionally, when we routinely screened for metabolic side effects, we found that treatment with the allosteric inhibitors WQ, NCT, and CBR alone did result in a significant reduction of mitochondrial OCR (**Figure 5C**), an effect that was not observed with the competitive inhibitor BI (**Figure 5C**). WQ and NCT also negatively affected TCA cycle activity as characterized by a reduction of M+2 isotopologue abundance of prominent TCA metabolites following [U-^{13}C]glucose tracing (**Figure 5D**). In contrast, BI had no adverse effect on TCA cycle activity or proliferation rate and emerged thus as the preferred PHGDH inhibitor in all subsequent experiments (**Figure 5D, S5A-D**). Combined treatment with the specific PHGDH inhibitor BI significantly reduced MTX-mediated cell migration (**Figure 5E**), which further indicates that mitochondrial SOC presents a metabolic foundation to support cancer cell motility upon cytosolic DHFR inhibition. This inhibitory effect on MTX-mediated cell motility is further intensified upon combined PHGDH inhibition and serine and glycine (S/G) starvation (**Figure 5F**). While serine and glycine starvation alone resulted only in moderate inhibitory effects on migration of MTX-treated cells, combined treatment with PHGDH inhibition fully blunted cell migration, indicating that serine is not only essential to support biomass production but also to support the metabolic program required for migration (**Figure 5F**). Furthermore, while neither BI treatment alone nor serine and glycine starvation alone were sufficient to prevent the induction of the previously observed EMT-phenotype in response to MTX (**Figure 2G, 5G**), combined inhibition and starvation did minimize ZEB1, ZEB2, and VIM upregulation (**Figure 5G**). This indicates that the efficient restriction of both, extracellular and *de novo*-synthesized serine to inhibit mitochondrial SOC, is effective to prevent the pro-migratory, phenotypic change upon MTX. Of note, it is also important to mention that serine and glycine starvation did not further increase

cell death after combined MTX and BI treatment (**Figure 5H**). As all cells exposed to MTX were already in full growth arrest, the additional perturbation with S/G starvation and/or PHGDH inhibition reveals that serine catabolism fulfills an important function to support cell motility. This function is independent of serine's anabolic function to support biosynthesis processes. (**Figure S5E**). Using the MTX-resistant MDA-MB468 cell line, we found that BI treatment is also sufficient to reduce the migratory capacity of such selected, pro-migratory, and potentially malignant cancer subpopulations (**Figure 5I**). In summary, through limiting the availability of *de novo*-synthesized serine using a specific PHGDH inhibitor, we uncovered that the mitochondrial SOC is essential to sustain full cancer cell migration under growth-arresting stimuli such as nucleotide synthesis inhibition by MTX. This implies that the mitochondrial SOC represents a metabolic liability to limit cell migration during certain chemotherapeutic interventions (**Figure 5J**).

Targeting mitochondrial serine catabolism reduces MTX-dependent cell motility

To further solidify the role of mitochondrial SOC as a keystone of sustained cell migration under nucleotide synthesis inhibition, we employed MDA-MB468 cells with a shRNA mediated knockdown (KD) of *MTHFD2,* a key enzyme of the mitochondrial SOC [39]. This mutant exhibited significantly reduced MTHFD2 expression (**Figure S6A**) and displayed a significant reduction of formate overflow even in the presence of MTX (**Figure 6A**), indicating effective abrogation of MTHFD2 activity. MTHFD2 knockdown did not significantly alter cell proliferation and both cell lines were comparatively sensitive to the growth-arresting effects of MTX (**Figure 6B**). We confirmed that MTX treatment itself did not upregulate protein levels of MTHFD2 or any of the other SOC enzymes SHMT1, SHMT2, or MTHFD1L (**Figure S6B-E**). In line with our prediction, MTHFD2 KD was sufficient to significantly reduce MTX-mediated cell motility (**Figure 6C**), confirming that mitochondrial SOC activity is a major metabolic determinant of cell migration in growth-arrested cells under MTX treatment. Of note, cell death rates upon MTX were not affected by MTHFD2 KD, which further confirms that the observed reduction upon MTX and MTHFD2 KD is not related to enhanced cell death or further reduced growth rates, but solely based on an inherent reduction of migratory capacity upon loss of mitochondrial SOC activity (**Figure 6B, 6D**). In summary, we uncovered that mitochondrial SOC acts as a metabolic facilitator of cell migration under stress conditions such as chemotherapeutic nucleotide-synthesis inhibition. Based on these observations, we speculate that different growth inhibiting and stress inducing conditions, such as antifolate therapy or energy limitation [4], can trigger increased rates of formate overflow and concomitant accumulation of formate within the tumor microenvironment. Such increased concentrations of formate might act in an autocrine and/or paracrine manner to trigger a pro-invasive phenotype, which represents the first stage to enter the metastasis process. Conclusively, targeting formate overflow emerges as a conceivable intervention to limit metastasis formation.

Genetic targeting of mitochondrial SOC reduces metastasis formation *in vivo*

We set thus out to test *in vivo* this concluding hypothesis on the central role of mitochondrial SOC as a facilitator of cancer cell migration and ultimately metastasis formation. To specifically inhibit formate overflow, we generated a stable knockdown of *Mthfd1l* in 4T1 breast cancer cells. The generated cells did show a functional knockdown of the enzyme as can be seen from the prominent reduction in formate release rates when compared to non-targeting shRNA transfected 4T1 cells (**Figure S7A**). In line with our previous reports [4, 10], knockdown of *Mthfd1l* had no effect on cell proliferation *in vitro* (**Figure S7B**) and reduced invasion (**Figure S7C**). To test if formate overflow suppression can reduce metastasis formation *in vivo*, we injected both murine

cell lines into the mammary fat pads of immune competent BALB/c mice and monitored primary tumor growth over 6 weeks (**Figure 7A**). As expected from the *in vitro* data, primary tumor growth *in vivo* and tumor weight at the endpoint were not affected by *Mthfd1l* knockdown (**Figure 7B, C**). After 6 weeks, mice were sacrificed and lung tissue was stained with H&E staining. Staining shows that micrometastases formation was visibly reduced in response to MTHFD1L KD (**Figure 7D**). In addition, the number of macroscopic lung metastases was counted and we found that primary tumors derived from 4T1 cells baring a knockdown for *Mthfd1l* did evoke significantly less pulmonary metastases compared to 4T1 cells expressing MTHFD1L (**Figure 7E**). While all mice that were injected with MTHFD1L-expressing 4T1 cells, exhibited lung metastases over 50% of mice injected with *Mthfd1l* knockdown cells did not show metastatic lesions (**Figure 7E**). These *in vivo* findings further strengthen the key relevance of mitochondrial SOC and especially mitochondrial formate generation as a cornerstone to support cancer cell migration independent of primary tumor growth and cancer cell proliferation rates.

Discussion

In this study, we uncovered a growth-independent function for serine and its mitochondrial catabolism that drives cancer cell dissemination. Importantly, by using MTX as a tool compound to study migration independent of proliferation, we could show that mitochondria sustain an autarkic SOC that is sufficient to support the cells migratory capacity. This finding implies the dismal possibility that chemotherapeutic approaches with nucleotide synthesis inhibiting drugs, which are undertaken to reduce primary cancer growth, might not sufficiently suppress the motility capacities of remaining cancer cells. The fact, that in our hands, breast cancer cells even showed a transitioning phenotype and were selected over time to be drug resistant, while at the same time showing enhanced migratory potential, could warrant further work to comparatively investigate metastatic disease progression after such therapies. Of note, apart from its use in oncologic treatment schemes, the antifolate MTX represents the anchor drug for chronic treatment of autoimmune diseases such as rheumatoid arthritis. Here, intracellular erythrocyte concentration of MTX and mean MTX plasma concentration after chronic, low-dose MTX were reported to be in a comparable, even slightly higher, nM range to our chosen drug concentration of 50 nM [40, 41]. This implies a potential significance of our findings also in cancer patients that are under chronic MTX therapy for an arthritic comorbidity and might warrant further clinical retrospective and prospective investigations beyond the scope of this study. Our aim here was however to more comprehensively analyze the metabolic pathways that foster such sustained cell migration under growth-arresting conditions. We previously reported that formate overflow via SOC is a characteristic of invasive cancer cells [10]. As, at the same time, it is well known that MTX has a direct inhibiting effect on SOC, this metabolic pathway emerged as a conceivable starting point for further mechanistic studies. Within SOC, the non-essential amino acid serine is catabolized in the mitochondrion to glycine and formyl-tetrahydrofolate (formyl-THF), which are required building blocks for cytosolic purine and thymidine (a pyrimidine) synthesis. During thymidine synthesis, the co-factor THF is oxidized to dihydrofolate (DHF), which subsequently requires regeneration to keep the folate in its bioactive form. This reduction of DHF to THF is dependent on the enzyme DHF reductase (DHFR), which is a target of MTX. Hence, upon MTX treatment the folate co-factor accumulates in its inactive form DHF, which prevents nucleotide synthesis and cell growth through obstruction of SOC activity [5] [42]. In accordance, our tool compound MTX effectively abolishes SOC-

dependent nucleotide synthesis in the cytosol. However, using [U^{13}C]serine- and [U^{13}C]glucose-assisted metabolic flux analyses, we found that mitochondrial one-carbon cycle is preserved under antifolate-induced nucleotide synthesis inhibition. Such compartmentalization of SOC is on the one hand enabled by the lack of oxidation of THF to DHF in the mitochondrial compartment, but is also based on the chemical modification of folate species and their transport activities across the mitochondrial membrane. For full biologic activity, folate species need to be polyglutamated by folylpolyglutamate synthase (FPGS) and the resulting polyglutamate species were shown to be poor substrates for transport across the mitochondrial membrane [43, 44]. Thus, polyglutamated folate species can be chemically trapped within the mitochondrion to sustain an autarkic mitochondrial SOC especially upon growth arrest and subsequently unaltered mitochondrial content. Furthermore, there have been implications that the mitochondrial folate transporter is specific for reduced folates with the result that MTX and folic acid itself might not be significantly transported across the mitochondrial membrane [45]. All in all, such compartmentalization of SOC and autarkic function of mitochondrial SOC emerges as a selective advantage upon perturbations of cytosolic SOC and indicates an additional metabolic functionality of the mitochondrial SOC pathway during growth-arresting conditions. Specifically, plastic serine catabolism through this sustained mitochondrial pathway could offer a metabolic reserve in the form of ATP and redox equivalent generation that might allow growth-arrested cancer cells to undergo an epithelial-mesenchymal transition and to enhance their migratory capacity to escape from sites of nutrient deprivation or chemotherapeutic targeting. Congruently, we could identify mitochondrial SOC as a targetable metabolic vulnerability by using genetic and pharmacologic inhibition of mitochondrial one-carbon cycle activity to reduce migration *in vitro* and metastasis formation *in vivo*. These findings are in line with previous reports indicating that serine *de novo* synthesis rates and serine uptake rates are associated with disease progression and even metastatic dissemination [11-13, 46]. But to our knowledge, this is the first report to show that it is truly the enhanced activity of mitochondrial serine catabolism to formate via SOC that translates these enhanced serine synthesis rates or serine uptake rates to a pro-migratory signal downstream. Based on these findings, we hypothesize that serine plasticity and the alternative usage of serine catabolism in the mitochondrion can selectively promote formate overflow in response to extrinsic or intrinsic stress stimuli such as growth inhibition or nutrient deprivation. In consequence, such increased local formate concentrations in the TME could subsequently serve as a local stress signal in an auto- or paracrine manner to promote the formation of invasive cancer cells. These cells are, as a result, more prone and capable to escape from a non-beneficial primary TME, which eventually advances dissemination and metastasis formation. Intervention with mitochondrial SOC at the root of this stress signaling cascade emerges as a promising, preventive strategy to hinder metastatic tumor progression early on.

Acknowledgment

We are grateful to Saverio Tardito (Cancer Research UK Beatson Institute, Glasgow, UK) for providing Plasmax medium to us. We are also thankful to Clément Thomas (LIH, Luxembourg) for providing 4T1 cells and to Patel's laboratory (Cambridge, UK) for providing HAP1 cells [38].

We would like to thank: the LCSB Metabolomics Platform, especially Xiangyi Dong and Floriane Vanhalle, for providing technical and analytical support; the National Cytometry Platform (Quantitative Biology Unit, LIH)

and especially Thomas Cerutti for support with flow cytometric analyses; all our collaboration partners for fruitful discussions and constructive feedback. All graphical figures were produced with BioRender.com.

J.M. is supported by the FNR-ATTRACT program (A18/BM/11809970), INTER-BMBF grant (18/13399110) and i2Tron (PRIDE19/14254520). N.K. is supported by the LIH Career Launchpad program (Legs Baertz). D.B. is supported by the FNR-ATTRACT program (A14/BM/7632103), the FNR-CORE (C18/BM/12691266), i2Tron (PRIDE19/14254520) and the FNR-RIKEN (TregBar/11228353) grant. D.B. and L.S.B. are funded by the FNR-PRIDE (PRIDE/11012546/NEXTIMMUNE) scheme. E.L. is supported by the FNR-CORE program (C16/BM/11282028 and C20/BM/14591557), by a Proof of Concept FNR grant (PoC/18/12554295), a PRIDE17/11823097 and by i2Tron (PRIDE19/14254520). G.D. and F.X. are supported by FNR-CORE (C17/BM/11642138). B.J. and M.Z.N. are supported by Luxembourg National Research Fund (C18/BM/12670304/COMBATIC) and FNRS Televie grant (7.4579.20).

Author Contributions

Conceptualization, J.M., N.K.; Methodology, J.M., N.K., C.J., M.Z.N., B.J., E.L., D.B., G.D., V.I.P.; Software, A.V., F.X.; Validation, N.K., J.M., L.N., C.D.; Formal Analysis, N.K., C.D., L.N., M.B., L.S.B., F.X., V.I.P., M.S., C.J.; Investigation, N.K., C.D., L.N., M.B., L.S.B., F.X., V.I.P., M.S., E.L.; Resources, C.J., A.V., J.M., E.L.; Data Curation, N.K., J.M., F.X., A.V.; Writing – Original Draft, N.K., J.M.; Writing – Review & Editing, All Authors; Visualization, N.K., J.M., L.S.B., F.X., V.I.P.; Supervision, J.M., D.B., A.V., E.L., G.D.; Project Administration, J.M., Funding Acquisition, J.M., D.B., E.L., A.V., G.D..

Materials & Methods

Chemicals

Methotrexate, rotenone, PKUMDL-WQ-2101, galactose, hydroxyurea, NAC, and fluorouracil were purchased from Sigma Aldrich. Clofarabine, pemetrexed disodium hydrate, sirolismus were purchased from Bio Connect. Simvastatin was purchased from Sanbio. CBR-5884 and BI-4916 were purchased from MedChemExpress. NCT-502 was purchased from ApeXBio.

Cell Culture

All cell lines were cultured in Dulbecco's modified Eagle's medium (DMEM) without phenol red, glucose, and glutamine (Thermo Fisher Scientific) and supplemented with 2 mM glutamine, 17 mM glucose, and 10 % fetal bovine serum (FBS) at 37°C and 5 % CO_2. For galactose treatment, supplemented glucose was replaced by 17 mM galactose at the beginning of the experiment. MDA-MB468 and LN229 were obtained from ATCC. HCT-116 were obtained from the group of E. Letellier (LSRU, University of Luxembourg), and 4T1 were obtained from C. Thomas (LIH, Luxembourg). HAP1 cells were obtained from Patel's laboratory [38] and cultured in IMDM medium supplemented with 10 % FBS. MTX-resistant MDA-MB468 cells were generated by chronic cultivation of MDA-MB468 cells with 50 nM MTX for 2 months until cells started to regrowth under MTX. All cell lines were regularly tested for mycoplasma contamination.

Metabolic Characterization

For metabolic characterization of cell lines, previously established protocols for absolute quantification of exchange fluxes and intracellular fluxes of one-carbon metabolism were applied [4].

Stable Isotope Tracing and Metabolite Extraction

Stable isotope tracing experiments with [U-^{13}C]-glucose tracer or [U-^{13}C]-glutamine tracer (Cambridge Isotope Laboratories, CLM-1396) were performed in DMEM supplemented with 2 mM glutamine, 17 mM glucose tracer, and 10 % FBS. Stable isotope tracing experiments with [U-^{13}C]-serine tracer (Cambridge Isotope Laboratories) were performed in MEM (Thermo Fisher Scientific) supplemented with 400 µM glycine, 2 mM glutamine, 17 mM glucose, 400 µM serine tracer, and 10 % FBS. To allow for adaptation, cells were cultivated in MEM for at least one passage prior to [U-^{13}C]-serine tracer experiments. 150,000 to 200,000 cells were seeded in 12-well plates in triplicates for each experimental condition. Identical triplicate wells were seeded to allow for cell count and cell volume determination (to calculate the packed cell volume (PCV)) at the start and end of each tracing experiment. The day after seeding, growth medium was replaced by tracer medium and cells were cultured for 24 h. In parallel, 3 wells per condition were counted to assess starting PCV. After 24 h, triplicate wells were counted to assess PCV at the end of the experiment and one set of triplicates was used for subsequent metabolite extraction. Medium of these triplicates was collected and analyzed for exchange rates. To determine the basal medium composition for the subsequent calculation of exchange rates, the identical medium was incubated in triplicates in empty 12 wells throughout the experiment and analyzed in parallel to the medium samples. Collected medium samples were centrifuged at 300 g for 5 min. Supernatant was collected and stored at -20°C until extraction of metabolites. Formate extraction, derivatization, and quantification as well as metabolite extraction for LC-MS analysis was performed as described in [4]. For metabolite extraction for GC-MS analysis after [U-^{13}C]-glucose tracing and [U-^{13}C]-glutamine tracing, cells were washed with cold 0.9 % NaCl solution. 400 µl ice-cold MeOH/H_2O_{MQ} [(ratio, 1:1) containing the internal standards pentanedioc-d6 acid and [U-^{13}C]-ribitol at a final concentration of 1 µg/ml and Tridecanoid-d25 acid at a final concentration of 5 µg/ml] was added to each well. Plates were incubated for 5 min at 4°C on a rocking shaker. Supernatant was collected, mixed with 200 µl $CHCl_3$, and centrifuged for 5 min at 13,000 g at 4°C. Upper polar phase was collected and stored at -20°C for subsequent MS analysis of polar metabolites.

GC-MS Measurements

Analysis of Formate Release Rates:

Formate derivatization in the culture medium was performed using MCF derivatization as described in [4]. GC-MS analysis was performed using an Agilent 7890A GC coupled to an Agilent 5975C inert XL Mass Selective Detector (Agilent Technologies). A sample volume of 1 µl was injected into a Split/Splitless inlet, operating in split mode (20:1) at 270 °C. The gas chromatograph was equipped with a 30 m (I.D. 250 µm, film 0.25 µm) DB-5MS capillary column (Agilent J&W GC Column, 122-5532G). Helium was used as carrier gas with a constant flow rate of 1.4 ml/min. GC oven temperature was held at 80 °C for 1 min and increased to 130 °C at 10 °C/min followed by a post run time of 4 min at 280 °C. Total run time was 15 min. Transfer line temperature was set to 280 °C. Mass selective detector (MSD) was operating under electron ionization at 70 eV. MS source was held at 230 °C and the quadrupole at 150 °C. For precise quantification, measurements were performed in selected ion monitoring mode. Target ions (*m/z*) and dwell times are shown in Table S2. GC-MS chromatograms were processed using Agilent MassHunter Quantitative Analysis for GC-MS, Version B.08.00. Final determination of release rates was performed as described in [4].

Determination of MIDs of Intracellular TCA Cycle Metabolites following Stable Isotope Tracing:

Polar metabolites were derivatized for 90 min at 45 °C with 20 µl of methoxyamine (c = 20 mg/ml) in pyridine under continuous shaking and subsequently for 90 min at 45 °C with 20 µl of MTBSTFA w/ 1% TBDMCS. GC-

MS analysis was performed using an Agilent 7890B GC coupled to an Agilent 5977A Mass Selective Detector (Agilent Technologies). A sample volume of 1 µl was injected into a Split/Splitless inlet, operating in splitless mode at 270 °C. Gas chromatograph was equipped with a 30 m (I.D. 250 µm, film 0.25 µm) ZB-35MS capillary column with 5 m guard column (Phenomenex). Helium was used as carrier gas with a constant flow rate of 1.2 ml/min. GC oven temperature was held at 100 °C for 2 min and increased to 300 °C at 10 °C/min and held for 4 min. Total run time was 26 min. Transfer line temperature was set to 280 °C. Mass selective detector (MSD) was operating under electron ionization at 70 eV. MS source was held at 230 °C and the quadrupole at 150 °C. For precise quantification of the MID, measurements were performed in selected ion monitoring mode. Target ions (*m/z*) and dwell times are shown in Table S3.

The MetaboliteDetector software package (Version 3.220180913) was used for mass spectrometric data post processing, quantification, MID calculations, correction of natural isotope abundance, and determinations of fractional carbon contributions [47].

Analysis of Medium Exchange Rates:

Polar metabolites of the culture medium were derivatized for 90 min at 45 °C with 20 µl of methoxyamine (c = 20 mg/ml) in pyridine under continuous shaking and subsequently for 90 min at 45 °C with 20 µl of MSTFA. GC-MS analysis was performed using an Agilent 7890B GC coupled to an Agilent 5977A Mass Selective Detector (Agilent Technologies). A sample volume of 1 µl was injected into a Split/Splitless inlet, operating in splitless mode at 270 °C. Gas chromatograph was equipped with a 30 m (I.D. 250 µm, film 0.25 µm) ZB-35MS capillary column with 5 m guard column (Phenomenex). Helium was used as carrier gas with a constant flow rate of 1.2 ml/min. GC oven temperature program: 90° C for 1 min, 9° C/min to 270° C, 25° C/min to 320° C and held for 7 min. Total run time was 30 min. Transfer line temperature was set to 280° C. MSD was operated under electron ionization at 70 eV. MS source was held at 230° C and the quadrupole at 150° C. Full scan mass spectra were acquired between m/z 70 and 700.

The MetaboliteDetector software package (Version 3.220180913) was used for quantification. Briefly, peak areas of all isotopologues of defined quantification ions were summed up and divided by the peak area of the internal standard for normalization. In addition, a calibration curve was prepared to calculate absolute concentrations. Absolute uptake and release rates were calculated as described in [4]

LC-MS Measurements

Untargeted LC-MS analysis was carried out as previously described in [4]. Targeted analysis of GSH/GSSG was performed as described in [48].

Nucleotide and NAD/NADH Analysis

The following analytical conditions are based on a protocol from [4]. Metabolite analyses were performed using a Thermo Vanquish Flex Quaternary LC coupled to a Thermo Q Exactive HF mass spectrometer. Chromatography was carried out with a SeQuant ZIC-pHILIC 5µm polymer (150 x 2.1 mm) column connected to the corresponding SeQuant ZIC-pHILIC Guard (20 x 2.1 mm) pre-column. Column temperature was maintained at 45 °C. The flow rate was set to 0.2 mL/min and the mobile phases consisted of 20 mmol/L ammonium carbonate in water, pH 9.2 (Eluent A) and Acetonitrile (Eluent B). The gradient was: 0 min, 80% B; 2 min, 80% B; 17 min, 20% B; 18 min 20% B; 19 min 80 % B; 20 min 80% B (0.4 mL/min); 24 min 80% B (0.4 mL/min); 24.5 min 80% B. The injection volume was 5 µL. All MS experiments were performed using electrospray ionization with polarity switching enabled (+ESI/-ESI). The source parameters were applied as

follows: sheath gas flow rate, 25; aux gas flow rate, 15; sweep gas flow rate, 0; spray voltage, 4.5 kV (+) / 3.5 kV (–); capillary temperature, 325 °C; S-lense RF level, 50; aux gas heater temperature, 50 °C. The Orbitrap mass analyzer was operated at a resolving power of 30,000 in full-scan mode (scan range: *m/z* 75…1000; automatic gain control target: 1e6; maximum injection time: 250 ms). Data were acquired with Thermo Xcalibur software (Version 4.3.73.11) and analyzed with TraceFinder (Version 4.1). Subsequent data analysis for normalization and natural isotope subtraction were performed using in house scripts as in [4].

Western Blot

Total cell lysates were prepared by 30 min incubation of cell pellets on ice in cell lysis buffer (150 mM NaCl, 1 mM EDTA, 50 mM Tris-HCl, 1% NP-40). Lysis efficiency was maximized by sonification. Lysis solution was centrifuged at 13,000 g for 15 min at 4°C and supernatant was collected and stored at -80°C. Protein concentration was determined by Bradford assay. 15 – 25 µg of total protein were loaded on NuPAGE 4-12% Bis-Tris gels (Life Technologies) or RunBlue 4-12% Bis-Tris gels (Westburg) using 4x NuPage LDS Sample buffer (Thermo Fisher Scientific) supplemented with 10 mM DTT (Sigma Aldrich) and blotted on nitrocellulose membrane according to standard protocols. Membranes were stained with REVERT staining solution (LI-COR) and analyzed for total protein abundance. Subsequently, membranes were blocked with Odyssey TBS blocking buffer (LI-COR) or 5% milk-powder in TBST and incubated with the indicated primary antibodies over night at 4°C. Incubation with secondary antibody occurred for 2 h at RT. Detection was performed with the Odyssey CLx Infrared Imaging System (LI-COR). ImageStudioLite Software Vers.5.2 (LI-COR) was used for image analysis. Antibodies used for Western blot analysis in this study: MTHFD1L (16113-1-AP) from Proteintech; vimentin (3390), β-actin (3700), and MTHFD2 (41377) from Cell Signaling Technology; PHGDH (HPA021241), PSAT1 (HPA042924), PSPH (HPA020376), SHMT1 (HPA023314), and SHMT2 (HPA020549) from Sigma Aldrich; IRDye 680RD Goat Anti-Mouse IgG (H+L) and IRDye 800CW Donkey Anti-Rabbit IgG (H+L) from LI-COR.

Poly-L-lysine Coating

Poly-L-lysine (P1274) was purchased from Sigma-Aldrich and reconstituted at 500 µg/ml in H_2O_{MQ}. Wells were coated with PLL prior to Seahorse measurement and migration analysis by Scratch assay. To this end, PLL solution was diluted 1:20 in H_2O_{MQ} and added to the plates at least 1 h prior to seeding. Following incubation with PLL and before cells were seeded, plates were washed twice with H_2O_{MQ} and allowed to dry under the hood.

Seahorse Measurements

The day prior to measuring OCR, 40,000 cells were seeded on poly-L-lysine coated plates. Cells were treated as indicated. XF96 Extracellular Flux Analyzer (Seahorse Bioscience) was used to measure basal OCR following manufacturer's instructions. Basal OCR was normalized to the protein concentration in the wells following the protocol described in [49] using Bradford assay.

Flow Cytometric Analysis of Cell Cycle Distribution and Cell Death

200,000 cells were seeded in 2 ml DMEM and treated the subsequent day as indicated. After incubation, medium was collected and cells were washed with PBS. PBS fraction was collected and cells were detached with trypsin. Trypsination was stopped by DMEM addition and this fraction as well as a subsequent PBS washing fraction were collected. The combined solutions were centrifuged and washed with PBS.

Cell Cycle Distribution

Anew centrifugation yielded a pellet that was resuspended in 100 µl PBS and fixed with ice-cold 80% EtOH. Fixed cells were stored at -20°C for at least 1 h and maximum 5 days prior to measurement. Cells were centrifuged, pellet was incubated for 1 h in 200 µl RNAse A in PBS (30 µg/ml) at RT. Immediately prior to measurement, 98 µl propidium iodide (PI) in PBS (50 µg/ml) was added. Flow cytometric analysis was performed using BD FACSCanto and BD FACSDiva software. Analysis was performed in FlowJo.

Cell Death Analysis

A new centrifugation yielded a pellet that was resuspended in 50 µl AnnexinV-FITC staining solution (5% AnnexinV-FITC in AnnexinV binding buffer (10 mM HEPES pH 7.4, 140 mM NaCl, 2.5 mM $CaCl_2$, 0.1% BSA in $_{dd}H2O$)) and incubated for 15 min on ice in the dark. 450 µl PI-staining solution (1.1 µg/ml PI in AnnexinV binding buffer) was added immediately prior to measurement using BD FACSCanto and BD FACSDiva software (for wild-type cells) or NovoCyte Quanteon (for GFP-positive transfected cells). Analysis was performed in FlowJo.

Flow Cytometric Analysis of ROS Levels

250,000 MDA-MB468 cells were seeded in 2 ml medium in 6 well plates and treated as indicated. Following incubation, adherent cells were detached with trypsin, centrifuged at 350 g for 5 min and washed with warm DMEM. Live cells were stained in 100 µl DMEM supplemented with 1:2,000 DAPI and 1:500 DCFDA for 30 min at 37°C. Following incubation, samples were centrifuged at 350 g for 5 min and washed with PBS. Following centrifugation at 350 g for 5 min, cells were resuspended in 100 µl PBS and measured using the BD LSRFortessa™ system and BD FACSDiva software. Data analysis was performed using FlowJo software.

Cell Proliferation

Cell proliferation was determined using the IncuCyte® Live-Cell Analysis system (Essen Bioscience). Cell proliferation was either determined as measurement of cell density (confluence) or and through quantification of red objects by using the IncuCyte ® NucLight Rapid Red Reagent (Essen Bioscience). Staining was performed according to manufacturer's instructions. Viable cell number was determined by trypan blue staining and automatic counting using a Countess™ Cell Counting Chamber Slide (Thermo Fisher).

Migration Assay (Wound Closure)

Cell migration was determined using the IncuCyte® Scratch Wound Assay system for 96 well plates (Essen Bioscience). 96 well image lock plates (Essen Bioscience) were PLL coated prior to seeding of 40,000 cells per well. Wound application was performed 24 h post seeding using the 96-pin IncuCyte WoundMaker Tool (Essen Bioscience) and indicated individual treatment conditions were applied simultaneously. Measurement for individual treatment conditions was performed in biological replicates (n = 4 – 8) and repeated as independent experiments as stated for the respective experiment (see figure legends).

Invasion and Migration Assay (Transwell Assay)

Cellular invasion and migration was analyzed by Boyden chamber assay as described in Meiser et al., 2018 [10]. Transwells were coated with ECM-Collagen for invasion assays and un-coated for migration assay. Treatment was carried out for 18 h to 24 h.

RNA Extraction, cDNA Synthesis, and qPCR Analysis

Total RNA was extracted directly from the cell culture dishes using RNeasy Mini Kit (Qiagen, 74104). For qPCR, RNA was converted to cDNA using High-capacity cDNA Reverse Transcription Kit (ThermoFisher, 4368814). qPCR was performed from 20 ng cDNA per samples using Fast SYBR™ Green Master Mix

(ThermoFisher, 4385612). All samples were analyzed in technical duplicates or triplicates. qPCR using Fast SYBR Green was conducted at 95°C for 20 s and then 40 cycles of 95°C for 1 s and 60°C for 20 s. Specificity of the reaction was verified by melt curve analysis. The relative quantification of each mRNA was performed using the comparative Ct method. Experiments were performed using the QuantStudio 5 Real-Time PCR System (Applied Biosciences, ThermoFisher Scientific) and data processing was performed using QuantStudio Design&Analysis v1.5.1 software (Applied Biosciences, ThermoFisher Scientific). All expression data was normalized to two housekeeping controls (*GAPDH* and *CycloA*). All human primers used in this study are listed in the table below:

Gene Name	Sequence Fwd (5' – 3')	Sequence Rev (5' – 3')
CDH1	AGTGCCAACTGGACCATTCA	TCTTTGACCACCGCTCTCCT
CycloA	CAGACAAGGTCCCAAAGACA	CCATTATGGCGTGTGAAGTC
GAPDH	CATGAGAAGTATGACAACAGCCT	AGTCCTTCCACGATACCAAAGT
MMP9	CGCGCTGGGCTTAGATCATT	GGTTCAGGGCGAGGACCATA
SLUG	CTACAGCGAACTGGACACACA	TGGAATGGAGCAGCGGTAGT
SNAIL	CGAAAGGCCTTCAACTGCAAA	TGACATCTGAGTGGGTCTGGA
VIM	CCTTGAACGCAAAGTGGAATC	GACATGCTGTTCCTGAATCTGAG
ZEB1	AAGAACTGCTGGGAGGATGACA	CCTCTTCAGGTGCCTCAGGAAAA
ZEB2	GCAAGAGGCGCAAACAAGC	GGGTTGGCAATACCGTCATCC

shRNA-mediated Gene Silencing

Gene knockdown with shRNA was performed in MDA-MB468 and 4T1 cells using lentiviral particles expressing two different shRNAs targeting the gene of interest and one non-silencing control vector (pGIPZ-shSCR: TTACTCTCGCCCAAGCGAG (Code: RHS4346). For silencing of the *MTHFD2* gene in MDA-MB468 cells, pGIPZ shMTHFD2-2: ATTGCATTTCTATTGGCCT (V2LHS_90968) purchased from Horizon Discovery was used. For silencing of the *Mthfd1l* gene in 4T1 cells, pGIPZ shMTHFD1L-2: TAGATTTCAATTTCATCTG (Code: V2LHS_96542) purchased from Horizon Discovery was used. All plasmids used for generation of lentivirus were first amplified from glycerol stocks, isolated (Machery&Nagel plasmid isolation kit), and used for transfection of HEK293T cells. Lentivirus was produced for 24 h in HEK293T cells co-transfected with the viral core packaging construct pCMVR8.74, the VSV-G envelope protein vector pMD2.G and the respective pGIPZ-shRNA-target plasmid using lipofectamine 3000 (Invitrogen #L3000008) as a transfection reagent. Filtered virus supernatant was used to transduce MDA-MB468 and 4T1 cells in DMEM supplemented with 2% FBS. After incubation at 37°C for 24 h, the virus was removed and cells were cultured in DMEM supplemented with 10 % FBS for 48 h. 96 h post transduction cells were cultured in selection media containing 2 µg/mL of puromycin (Sigma #P8833) for five passages to obtain stably transduced GFP-positive cells.

Animal Model

Animal experiments were performed according to all applicable laws and regulations, after receiving approval by the institution's Animal Experimentation Ethics Committee at UL (AEEC) and the veterinarian service of the Ministry of Agriculture, Viniculture & Rural Development (TumorMetab LUPA 2020/01). They ensure that care and use of animals for research purposes was conducted according to the EU Directive 2010/63/EU, as well as the Grand-Ducal Regulation of January 11, 2013 on the protection of animals used for scientific purposes. These included the justification of the use of animals, their welfare and the incorporation of the principles of the 3R's (Replacement, Reduction and Refinement). A biostatistician reviewed all animal protocols. Mice were

housed in a specific pathogen free (SPF) facility at a relative humidity of 40–70%, at 22 °C, and in 12 h dark/light cycles.

Syngeneic 4T1 mammary carcinoma cells were orthotopically implanted into the left mammary fat pads (1 injection/mouse) of immune competent female Balb/c mice according to established protocols [50]. Briefly, each injection contained 2.000 cells in a mixture of 25 µL PBS and 25 µL matrigel. 9 mice per group were injected with either 4T1 SCR or 4T1 *MTHFD1L* KD cells. Primary tumor growth was monitored between day 7 and day 35 of the experiment. Weight was monitored over time and no weight loss was observed. Experiment was terminated after 6 weeks and lung and liver were prepared for examination of metastatic outgrowth. No metastases were found in the liver. Macroscopic lung metastases were blindly counted under a microscope and microscopic lung metastases were visualized by H&E staining.

H&E staining

For H&E staining, snap-frozen lungs were cut in 15 µm sections using Leica Cryostat (Leica Biosystems) and embedded in Tissue-Tek® O.C.T (Sakura). 5 sections in a distance of 150 µm to each other were stained per lung. Staining was performed according to established protocols. Briefly, selected sections were dehydrated with MeOH and stained with Gill 2 hematoxylin. Sections were neutralized with successive washes of tap water, hard water (10g MgSO4 and 0.7g NaHCO3 per L), and distilled water. Subsequently, sections were stained with Eosin-solution and dehydrated through successive washes with 80%, 95%, 100% EtOH, and Xylol prior to mounting.

Proteomics

SILAC (Stable Isotope Labeling with Amino acids in Cell culture) strategy was used for the proteomic analysis. In general, MDA-MB468 cells were cultivated in DMEM-F12 SILAC medium supplemented either with Lys^0 and Arg^0 (light channel) or Lys^8 and Arg^{10} (heavy channel). After 6 passages, labeling efficiency of heavy channel was checked using LC-MS/MS. Cells in light channel were treated with 50 nM MTX for 24h and 72h, while heavy channel was used as control. Cell pellets of biological duplicates were collected after the treatment. Proteins were extracted in lysis buffer (50mM ammonium bicarbonate, 6M Urea, 2M Thio-urea, pH 8) following a 30 min incubation at 4 °C in the presence of protease inhibitors (cOmplete™ EDTA-free Protease Inhibitor Cocktail, Roche). Following a centrifugation at 16,000 g for 10 min, supernatants were taken for protein quantification. Samples from light channel (50 µg protein) were mixed with control heavy channel (50 µg protein) for protein reduction (5 mM DTT, 1 h incubation at 37°C) and alkylation (10 mM IAA, 45min in dark at room temperature). Protein digestion was performed with Lys-C (FUJIFILM Wako, 125-05061) at 1:30 ratio (enzyme/protein substances) for 4 h at 37 °C, then samples were diluted 4 times with 50 mM ammonium bicarbonate and digested overnight with 1 µg of trypsin at 37 °C. Digestion was terminated through addition of formic acid (1% final concentration). Digested peptides were cleaned up with reverse phase Sep-Pak C18 1 cc Vac Cartridge (Waters, WAT054955) and eluted with 1 mL 50% ACN. Eluted peptides were dried by Speedvac (Thermo Fisher Scientific) and re-suspended in 0.1% formic acid. Peptide concentration was measured with Nanodrop. Peptides were measured by LC-MS/MS on Q-Exactive HF mass spectrometer (Thermo Fisher) connected to a Dionex Ultimate 3000 (Thermo Fisher). 500 ng of peptides were loaded onto a trap column (Acclaim PepMap 75 µm x 2 cm, C18, 3 µm) and separated on a 25 cm Acclaim pepmap RSLC column (75 µm x 25 cm, C18, 2 µm) using a 150 min gradient (2% to 90% acetonitrile) with a flow rate of 0.3 µL/min. MS data were acquired in data dependent mode (DDA). Survey scans of peptide precursors from 375

to 1500 m/z were performed at 70,000 resolution with a 3×10^6 ion count target and the top 12 abundant peaks from survey scan were selected for fragmentation. Tandem MS was performed by isolation at 1.4 m/z with the quadrupole, HCD fragmentation with a normalized collision energy of 28. The MS2 ion count target was set to 1×10^5 and the max injection time was 45 ms. Only precursors with a charge state of 2–7 were sampled for MS2. The dynamic exclusion duration was set to 20 s with a 10 ppm mass tolerance around the selected precursor and its isotopes. Each sample was analyzed twice as technical replicates. All raw data was analyzed with MaxQuant (version 1.6.7.0) and searched with Andromeda against the mus musculus database from Uniprot. The minimal peptide length was set to 7 amino acids and the maximum of 3 missed cleavages were allowed. The search included variable modifications of methionine oxidation and N-terminal acetylation, deamidation (N and Q) and fixed modification of carbamidomethyl cysteine. The “Match between run” was checked within 1 min retention time window. Mass tolerance for peptide precursor and fragments were set as 10 ppm and 20 ppm, respectively. The FDR was set to 0.01 for peptide and protein identifications. SILAC based protein quantification (MaxQuant built-in) was used for quantitative evaluation of identified protein. ProTIGY (https://github.com/broadinstitute/protigy), an R based tool, was used for differential analysis of MaxQuant output.

Statistics

Unpaired *t*-test with Welch’s correction was applied for pairwise comparison using GraphPad Software Vers.8. For normalization, data points of one experiment were either normalized to the untreated control or divided by the global mean of this individual experiment. We define one *n* as one independent biological experiment (consisting of several wells, e.g. triplicate wells for all stable isotope tracing experiments). The mean of one experiment was considered as one *n*. The mean values of several independent experiments (as indicated in figure legends) were plotted and used for statistical analysis as indicated.

References

1. Siegel, R.L., K.D. Miller, and A. Jemal, *Cancer statistics, 2019.* CA Cancer J Clin, 2019. **69**(1): p. 7-34.
2. DeBerardinis, R.J. and N.S. Chandel, *Fundamentals of cancer metabolism.* Sci Adv, 2016. **2**(5): p. e1600200.
3. Bergers, G. and S.M. Fendt, *The metabolism of cancer cells during metastasis.* Nat Rev Cancer, 2021.
4. Meiser, J., et al., *Serine one-carbon catabolism with formate overflow.* Sci Adv, 2016. **2**(10): p. e1601273.
5. Tibbetts, A.S. and D.R. Appling, *Compartmentalization of Mammalian folate-mediated one-carbon metabolism.* Annu Rev Nutr, 2010. **30**: p. 57-81.
6. Benzarti, M., et al., *Metabolic Potential of Cancer Cells in Context of the Metastatic Cascade.* Cells, 2020. **9**(9).
7. Elia, I., G. Doglioni, and S.M. Fendt, *Metabolic Hallmarks of Metastasis Formation.* Trends Cell Biol, 2018. **28**(8): p. 673-684.
8. Faubert, B., A. Solmonson, and R.J. DeBerardinis, *Metabolic reprogramming and cancer progression.* Science, 2020. **368**(6487).
9. LeBoeuf, S.E., et al., *Activation of Oxidative Stress Response in Cancer Generates a Druggable Dependency on Exogenous Non-essential Amino Acids.* Cell Metab, 2020. **31**(2): p. 339-350 e4.
10. Meiser, J., et al., *Increased formate overflow is a hallmark of oxidative cancer.* Nat Commun, 2018. **9**(1): p. 1368.
11. Pollari, S., et al., *Enhanced serine production by bone metastatic breast cancer cells stimulates osteoclastogenesis.* Breast Cancer Res Treat, 2011. **125**(2): p. 421-30.
12. Rossi, M., et al., *Heterogeneity in PHGDH protein expression potentiates cancer cell dissemination and metastasis.* bioRxiv, 2021: p. 2021.01.24.427949.

13. Samanta, D., et al., *PHGDH Expression Is Required for Mitochondrial Redox Homeostasis, Breast Cancer Stem Cell Maintenance, and Lung Metastasis.* Cancer Res, 2016. **76**(15): p. 4430-42.
14. Ngo, B., et al., *Limited Environmental Serine and Glycine Confer Brain Metastasis Sensitivity to PHGDH Inhibition.* Cancer Discov, 2020. **10**(9): p. 1352-1373.
15. Hryniuk, W., *Mechanism of Action of Methotrexate.* Proceedings of the American Association for Cancer Research, 1974. **15**(Mar): p. 136-136.
16. Stoller, R.G., et al., *Use of plasma pharmacokinetics to predict and prevent methotrexate toxicity.* N Engl J Med, 1977. **297**(12): p. 630-4.
17. Chabner, B.A. and R.C. Young, *Threshold methotrexate concentration for in vivo inhibition of DNA synthesis in normal and tumorous target tissues.* J Clin Invest, 1973. **52**(8): p. 1804-11.
18. Huang, S., et al., *Study on Relationships of Tumor Status and Gene Polymorphism With Blood Concentration of MTX and Toxicities in 63 Pediatric Mature B Cell Lymphoma in Chinese Population.* Technol Cancer Res Treat, 2021. **20**: p. 1533033821995288.
19. Kawakatsu, S., et al., *Population pharmacokinetic analysis of high-dose methotrexate in pediatric and adult oncology patients.* Cancer Chemother Pharmacol, 2019. **84**(6): p. 1339-1348.
20. Garcia-Sanchez, A., A.G. Miranda-Diaz, and E.G. Cardona-Munoz, *The Role of Oxidative Stress in Physiopathology and Pharmacological Treatment with Pro- and Antioxidant Properties in Chronic Diseases.* Oxid Med Cell Longev, 2020. **2020**: p. 2082145.
21. Phillips, D.C., K.J. Woollard, and H.R. Griffiths, *The anti-inflammatory actions of methotrexate are critically dependent upon the production of reactive oxygen species.* Br J Pharmacol, 2003. **138**(3): p. 501-11.
22. Babiak, R.M., et al., *Methotrexate: pentose cycle and oxidative stress.* Cell Biochem Funct, 1998. **16**(4): p. 283-93.
23. Nguyen, H.L., et al., *Oxidative stress and prostate cancer progression are elicited by membrane-type 1 matrix metalloproteinase.* Mol Cancer Res, 2011. **9**(10): p. 1305-18.
24. Rhyu, D.Y., et al., *Role of reactive oxygen species in TGF-beta1-induced mitogen-activated protein kinase activation and epithelial-mesenchymal transition in renal tubular epithelial cells.* J Am Soc Nephrol, 2005. **16**(3): p. 667-75.
25. Chen, D., et al., *MiR-373 drives the epithelial-to-mesenchymal transition and metastasis via the miR-373-TXNIP-HIF1alpha-TWIST signaling axis in breast cancer.* Oncotarget, 2015. **6**(32): p. 32701-12.
26. Reczek, C.R. and N.S. Chandel, *ROS-dependent signal transduction.* Curr Opin Cell Biol, 2015. **33**: p. 8-13.
27. Hunter, M.V., et al., *Oxidative Stress Orchestrates Cell Polarity to Promote Embryonic Wound Healing.* Dev Cell, 2018. **47**(3): p. 377-387 e4.
28. Porporato, P.E., et al., *A mitochondrial switch promotes tumor metastasis.* Cell Rep, 2014. **8**(3): p. 754-66.
29. Piperigkou, Z., et al., *Key Matrix Remodeling Enzymes: Functions and Targeting in Cancer.* Cancers (Basel), 2021. **13**(6).
30. Klein, E.A., et al., *Vitamin E and the risk of prostate cancer: the Selenium and Vitamin E Cancer Prevention Trial (SELECT).* JAMA, 2011. **306**(14): p. 1549-56.
31. Lignitto, L., et al., *Nrf2 Activation Promotes Lung Cancer Metastasis by Inhibiting the Degradation of Bach1.* Cell, 2019. **178**(2): p. 316-329 e18.
32. Vazquez, A., et al., *Catabolic efficiency of aerobic glycolysis: The Warburg effect revisited.* BMC Syst Biol, 2010. **4**: p. 58.
33. Morscher, R.J., et al., *Mitochondrial translation requires folate-dependent tRNA methylation.* Nature, 2018. **554**(7690): p. 128-132.
34. Diehl, F.F., et al., *Cellular redox state constrains serine synthesis and nucleotide production to impact cell proliferation.* Nat Metab, 2019. **1**(9): p. 861-867.
35. Palm, W. and C.B. Thompson, *Nutrient acquisition strategies of mammalian cells.* Nature, 2017. **546**(7657): p. 234-242.
36. Vande Voorde, J., et al., *Improving the metabolic fidelity of cancer models with a physiological cell culture medium.* Sci Adv, 2019. **5**(1): p. eaau7314.
37. Ducker, G.S., et al., *Reversal of Cytosolic One-Carbon Flux Compensates for Loss of the Mitochondrial Folate Pathway.* Cell Metab, 2016. **24**(4): p. 640-641.
38. Burgos-Barragan, G., et al., *Mammals divert endogenous genotoxic formaldehyde into one-carbon metabolism.* Nature, 2017. **548**(7669): p. 549-554.
39. Zheng, Y., et al., *Mitochondrial One-Carbon Pathway Supports Cytosolic Folate Integrity in Cancer Cells.* Cell, 2018. **175**(6): p. 1546-1560 e17.
40. den Boer, E., et al., *Determinants of erythrocyte methotrexate polyglutamate levels in rheumatoid arthritis.* J Rheumatol, 2014. **41**(11): p. 2167-78.

41. Zhu, T., et al., *Investigation of Potential Drug-Drug Interactions between Peficitinib (ASP015K) and Methotrexate in Patients with Rheumatoid Arthritis.* Clin Drug Investig, 2020. **40**(9): p. 827-838.
42. Garcia-Martinez, L.F. and D.R. Appling, *Characterization of the folate-dependent mitochondrial oxidation of carbon 3 of serine.* Biochemistry, 1993. **32**(17): p. 4671-6.
43. Lawrence, S.A., et al., *Mammalian mitochondrial and cytosolic folylpolyglutamate synthetase maintain the subcellular compartmentalization of folates.* J Biol Chem, 2014. **289**(42): p. 29386-96.
44. Lowe, K.E., et al., *Regulation of folate and one-carbon metabolism in mammalian cells. II. Effect of folylpoly-gamma-glutamate synthetase substrate specificity and level on folate metabolism and folylpoly-gamma-glutamate specificity of metabolic cycles of one-carbon metabolism.* J Biol Chem, 1993. **268**(29): p. 21665-73.
45. Horne, D.W., R.S. Holloway, and H.M. Said, *Uptake of 5-formyltetrahydrofolate in isolated rat liver mitochondria is carrier-mediated.* J Nutr, 1992. **122**(11): p. 2204-9.
46. Tajan, M., et al., *Serine synthesis pathway inhibition cooperates with dietary serine and glycine limitation for cancer therapy.* Nat Commun, 2021. **12**(1): p. 366.
47. Hiller, K., et al., *MetaboliteDetector: comprehensive analysis tool for targeted and nontargeted GC/MS based metabolome analysis.* Anal Chem, 2009. **81**(9): p. 3429-39.
48. Mak, T.W., et al., *Glutathione Primes T Cell Metabolism for Inflammation.* Immunity, 2017. **46**(6): p. 1089-1090.
49. Dranka, B.P., et al., *Assessing bioenergetic function in response to oxidative stress by metabolic profiling.* Free Radic Biol Med, 2011. **51**(9): p. 1621-35.
50. Kocaturk, B. and H.H. Versteeg, *Orthotopic injection of breast cancer cells into the mammary fat pad of mice to study tumor growth.* J Vis Exp, 2015(96).

Figure 1

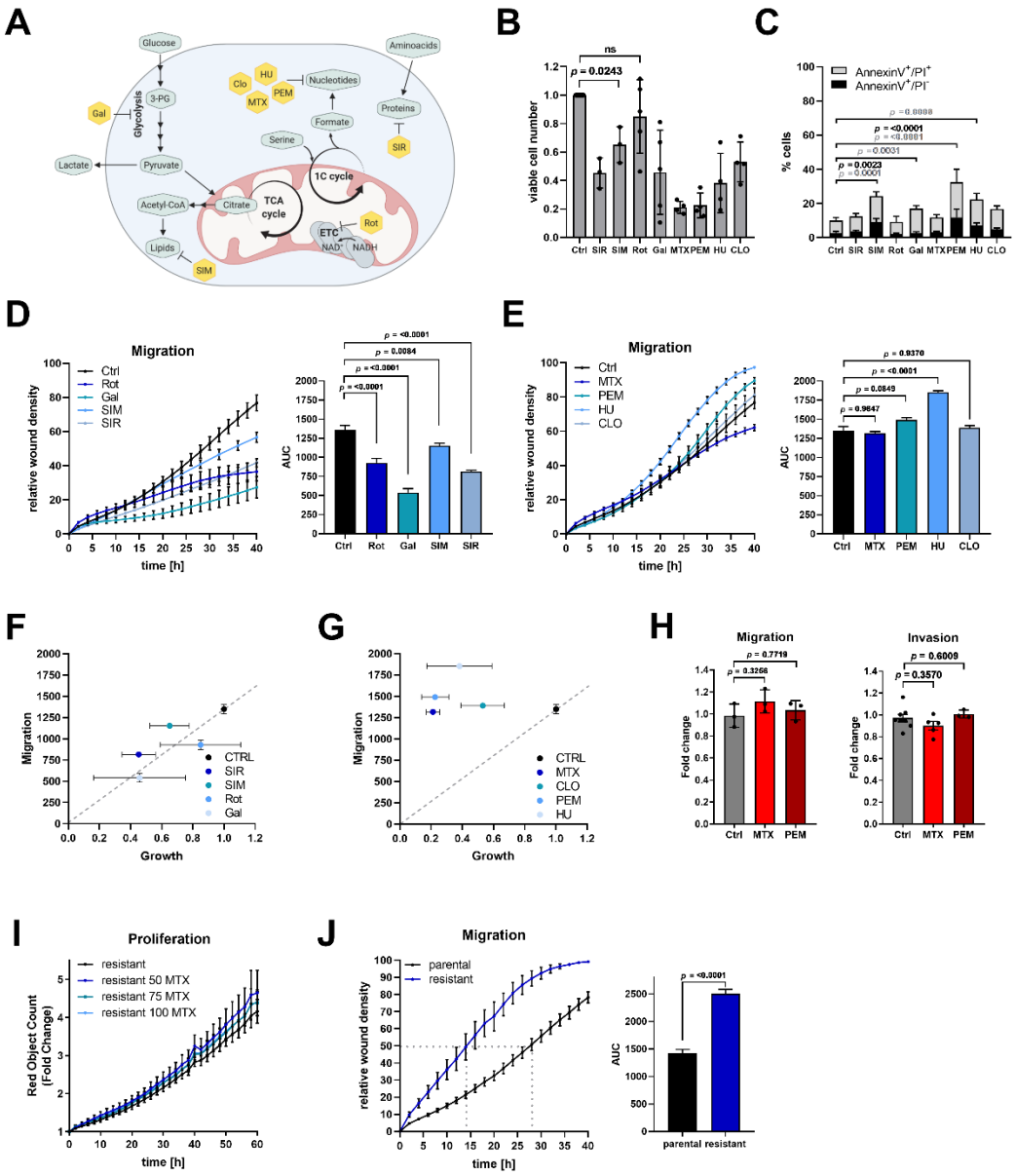

Figure 1: Inhibition of major anabolic synthesis routes differentially impacts the motility potential of cancer cells. (A) Schematic depicting synthesis routes of central metabolic building blocks (lipids, nucleotides, and proteins) and pharmacologic intervention points of the selected drug panel. **(B)** MDA-MB468 cells were treated with 100 nM Sirolimus (SIR), 1 µM Simvastatin (SIM), 50 nM Rotenone (Rot), galactose (Gal) supplementation, 50 nM Methotrexate (MTX), 1 µM Pemetrexed (PEM), 0.5 mM hydroxyurea (HU), and 100 nM Clofarabine (CLO) for 48 h. Viable cell number was determined by trypan blue staining. Each dot represents an independent experiment; mean ± SD; ordinary one-way ANOVA with Dunnett's multiple comparisons test. Comparisons to control apart from the labeled are all significant with p<0.0001. **(C)** MDA-MB468 cells were treated for 48 h as in (B). Cell death induction was assessed by flow cytometric analysis of AnnexinV-FITC/PI-stained cells; mean ± SD (n = 3 - 8). 2way ANOVA with Dunnett's multiple comparisons test. **(D)** Migration of MDA-MB468 cells in response to 50 nM Rot, Gal, 1 µM SIM, and 100 nM SIR and respective area under curve (AUC); mean ± SEM (n = 3 - 9); Brown-Forsythe and Welch one-way ANOVA with Dunnett's multiple comparisons test. **(E)** Migration of MDA-MB468 cells in response to 50 nM MTX, 1 µM PEM, 0.5 mM HU, and 100 nM CLO and respective AUC; mean ± SEM (n = 3 - 12); Brown-Forsythe and Welch one-way ANOVA with Dunnett's multiple comparisons test. **(F)** Correlation of cell migration assessed as AUC over 40h and proliferation assessed as fold cell growth after 48 h compared to control. MDA-MB468 cells were treated as in (B) and (D). **(G)** Correlation of cell migration assessed as AUC over 40h and proliferation assessed as fold cell growth after 48 h compared to control. MDA-MB468 cells were treated as in (B) and (E). **(H)** Migration and invasion of MDA-MB468 cells treated for 24 h with 50 nM MTX was assessed using non-coated (migration) or ECM-Collagen-coated (invasion) Boyden chambers. Each dot represents an independent experiment; mean ± SEM; Brown-Forsythe and Welch one-way ANOVA with Dunnett's multiple comparisons test. **(I)** Proliferation of MTX-resistant MDA-MB468 cells upon the indicated concentrations of MTX [nM] measured as cell density; mean ± SEM (n = 4). **(J)** Migration of parental and MTX-resistant MDA-MB468 cells and respective AUC; mean ± SEM (n = 6 - 15); unpaired t-test with Welch's correction. For comparison, the time point of 50% wound closure is indicated for both cell lines.

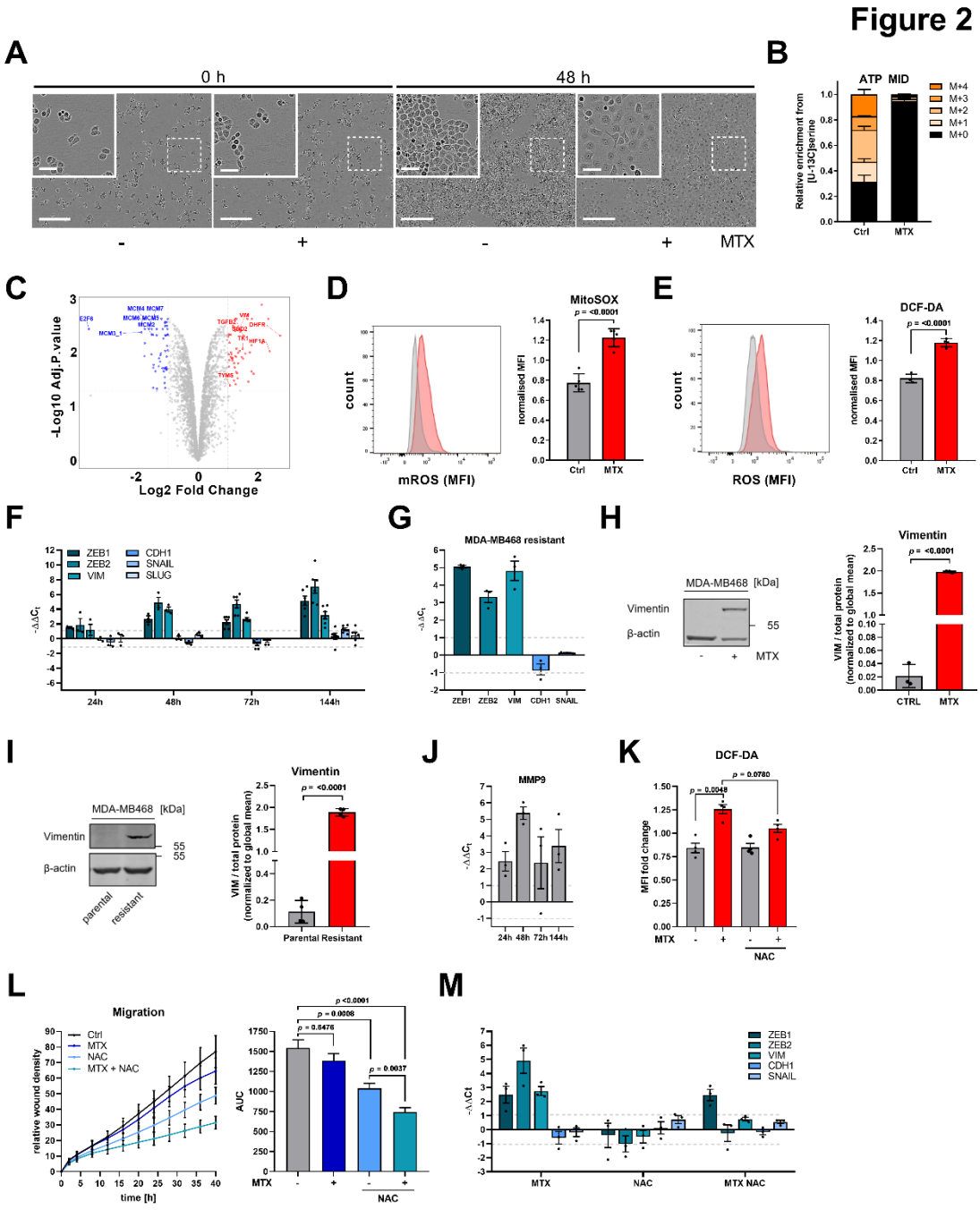

Figure 2: MTX treatment triggers a ROS-driven EMT phenotype. (A) Morphological changes of MDA-MB468 cells in response to 48 h 50 nM MTX. Pictures are representative of independent experiments. Scale bars correspond to 60 and 300 µm. **(B)** MID of intracellular ATP upon [U-^{13}C]serine tracer in response to 24 h 50 nM MTX in MDA-MB468 cells. Graph shows mean ± SEM of five independent experiments each measured in triplicate wells. **(C)** Quantitative proteomics analysis of SILAC-labeled MDA-MB468 cells treated with and without 50 nM MTX for 72h. The right side of the volcano plot shows the upregulated proteins after MTX treatment (red), while downregulated ones on the left side (blue). Differential expressions were defined as absolute log2 Fold change ≥ 1 with adjusted p-value ≤ 0.05. **(D)** Mitochondrial ROS levels in response to 24 h 50 nM MTX measured by flow cytometric quantification of MitoSOX mean fluorescence intensity. Each dot represents an independent experiment; mean ± SD; unpaired t-test with Welch's correction. **(E)** Intracellular ROS levels in response to 24 h 50 nM MTX measured by flow cytometric quantification of DCF-DA mean fluorescence intensity. Each dot represents an independent experiment; mean ± SD; unpaired t-test with Welch's correction. **(F)** mRNA expression from the indicated target genes in MDA-MB468 cells in response to 50 nM MTX at the indicated time points as measured using real-time RT-qPCR. Each dot represents an independent experiment; mean ± SEM. No data shown for *SLUG* expression at 72 h. **(G)** mRNA expression from the indicated target genes in MTX-resistant MDA-MB468 cells relative to parental MDA-MB468 cells as measured using real-time RT-qPCR. Each dot represents an independent experiment; mean ± SEM. **(H)** Expression of vimentin in MDA-MB468 cells after 240 h 50 nM MTX treatment; β-actin serves as loading control. Quantification of vimentin signal intensity relative to total protein stain. Each dot represents an independent experiment; mean ± SD; unpaired t-test with Welch's correction. **(I)** Expression of vimentin in parental and MTX-resistant MDA-MB468 cells; β-actin serves as loading control. Quantification of vimentin signal intensity relative to total protein stain. Each dot represents an independent experiment; mean ± SD; unpaired t-test with Welch's correction. **(J)** mRNA expression from

MMP9 in MDA-MB468 cells in response to 50 nM MTX at the indicated time points as measured using real-time RT-qPCR. Each dot represents an independent experiment; mean ± SEM. **(K)** Intracellular ROS levels in response to 24 h 50 nM MTX and 10 mM NAC as measured by flow cytometric quantification of DCF-DA mean fluorescence intensity. Each dot represents an independent experiment. Graph shows mean ± SD; Brown-Forsythe and Welch ANOVA test with Games-Howell's multiple comparisons test. **(L)** Migratory potential of MDA-MB468 cells in response to 10 mM NAC and 50 nM MTX treatment as time-dependent quantification of relative wound density in IncuCyte and respective AUC. Graph shows mean ± SEM (n = 3); Brown-Forsythe and Welch ANOVA test with Games-Howell's multiple comparisons test. **(M)** mRNA expression from the indicated target genes in MDA-MB468 cells in response to 10 mM NAC and 50 nM MTX at 72 h as measured using real-time RT-qPCR. Each dot represents an independent experiment; mean ± SEM.

Figure 3

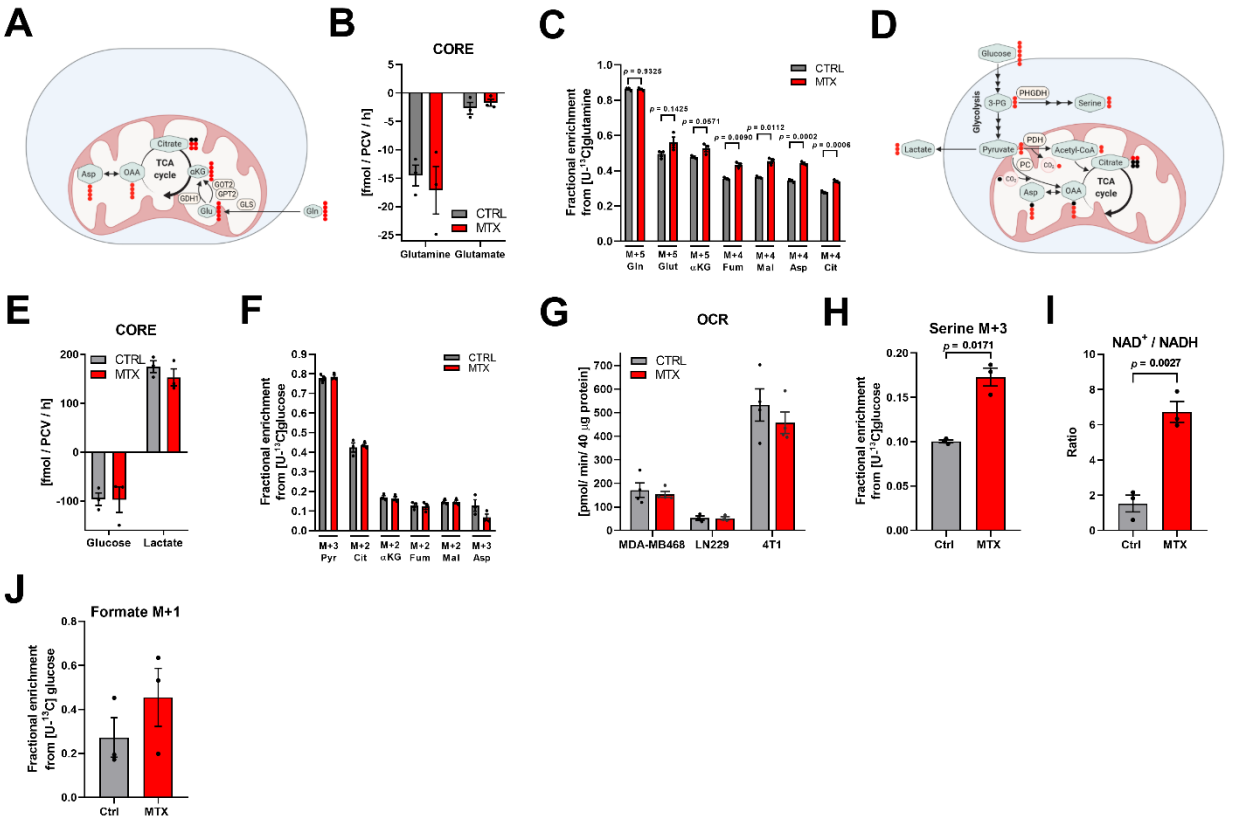

Figure 3: MTX-treated cells sustain high metabolic rates and enhance *de novo* serine synthesis. (A) Schematic depicting interdependence of glycolysis and tricarboxylic acid (TCA) cycle as well as metabolic ^{13}C label pattern from [U-^{13}C]glutamine tracer. **(B)** Absolute consumption and release (CORE) rates of glutamine and glutamate in the culture medium from MDA-MB468 cells in response to 24 h 50 nM MTX. Each dot represents an individual experiment composed of triplicate wells; mean ± SEM. **(C)** Enrichment of representative isotopomers of glutamine (Gln), glutamate (Glut), α-ketoglutarate (αKG), fumarate (Fum), malate (Mal), aspartate (Asp), and citrate (Cit) upon [U-^{13}C]glutamine tracer in response to 24 h 50 nM MTX in MDA-MB468 cells. Each dot represents an independent experiment in triplicate wells; mean ± SEM; unpaired t-test with Welch's correction. **(D)** Schematic depicting interdependence of glycolysis and TCA cycle as well as expectable metabolic ^{13}C label pattern from [U-^{13}C]glucose tracer. **(E)** Absolute CORE rates of lactate and glucose in the culture medium of MDA-MB468 cells in response to 24 h 50 nM MTX. Each dot represents an individual experiment composed of triplicate wells; mean ± SEM. **(F)** Enrichment of representative isotopologues of pyruvate (Pyr), Cit, αKG, Fum, Mal, and Asp upon [U-^{13}C]glucose tracer in response to 24 h 50 nM MTX in MDA-MB468 cells. Each dot represents an independent experiment with triplicate wells; mean ± SEM; unpaired t-test with Welch's correction. **(G)** Basal cellular respiration in response to 24 h 50 nM MTX treatment was determined in MDA-MB468, LN229, and 4T1 cells as quantification of mitochondrial oxygen consumption rate (OCR). Each dot represents an individual experiment composed of six technical replicates; mean ± SEM. **(H)** Enrichment of M+3 isotopologue of serine upon [U-^{13}C]glucose tracer in response to 24 h 50 nM MTX in MDA-MB468 cells. Each dot represents an independent experiment in triplicate wells; mean ± SEM; unpaired t-test with Welch's correction. **(I)** Ratio of absolute intracellular NAD+ to NADH in MDA-MB468 cells in response to 24 h 50 nM MTX. Each dot represents an individual experiment composed of triplicate wells; mean ± SEM. **(J)** M+1 isotopologue of extracellular formate in MDA-MB468 cells using [U-^{13}C]glucose tracer upon 24 h treatment with 50 nM MTX. Each dot indicates an independent experiment measured in triplicate wells; mean ± SEM.

Figure 4

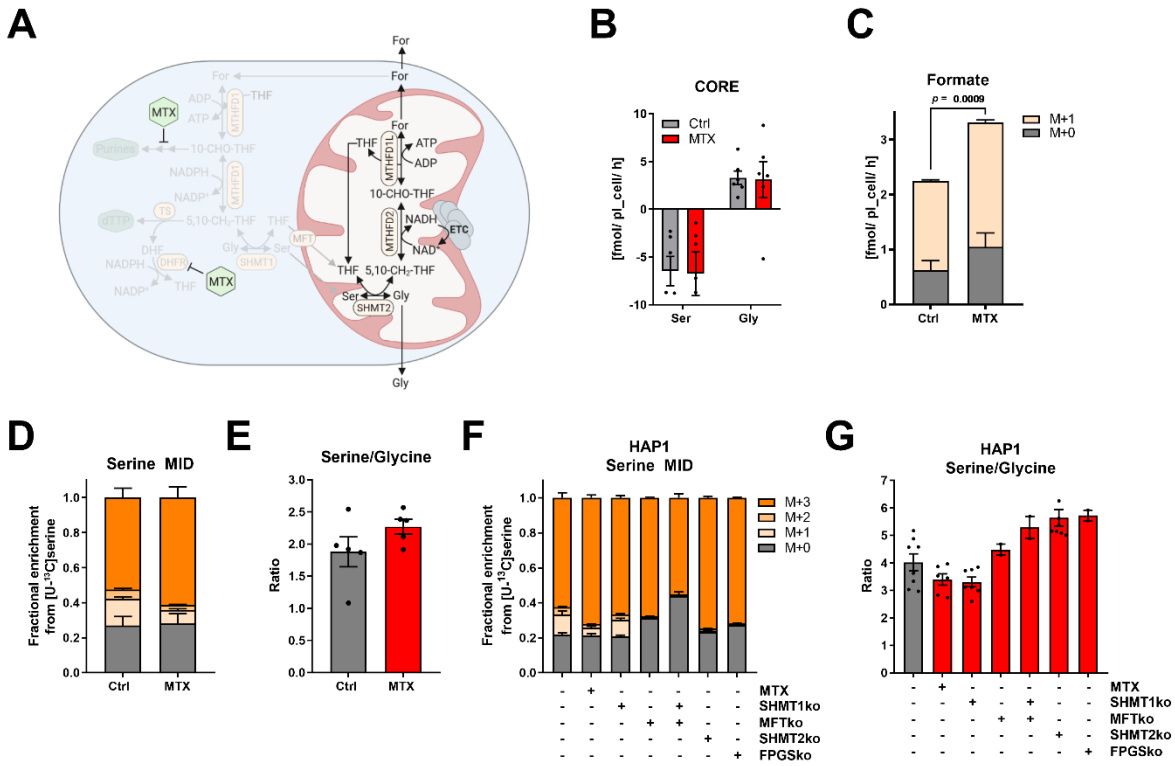

Figure 4: Mitochondria protect SOC-dependent serine catabolism in the presence of MTX. (A) Schematic of the cytosolic and mitochondrial compartments of SOC and the pharmacologic intervention points of MTX. **(B)** Absolute CORE rates of serine and glycine of MDA-MB468 cells in response to 24 h 50 nM MTX. Each dot represents the mean of an individual experiment each measured in triplicate wells; mean ± SEM. **(C)** MID of extracellular formate upon [U-^{13}C]serine tracer in MDA-MB468 cells in response to 24 h 50 nM MTX. Graph shows mean ± SEM of three independent experiments each measured in triplicate wells; unpaired t-test with Welch's correction for M+1 isotopologue enrichment. **(D)** MID of intracellular serine upon [U-^{13}C]serine tracer in MDA-MB468 cells in response to 24 h 50 nM MTX; mean ± SEM of four independent experiments each measured in triplicate wells. **(E)** Ratio of absolute intracellular serine and glycine in response to 24 h 50 nM MTX in MDA-MB468 cells. Each dot represents an independent experiment in triplicate wells; mean ± SEM. **(F)** MID of intracellular serine upon [U-^{13}C]serine tracer in SHMT1, MFT, SHMT2, and FPGS-depleted HAP1 cells; mean ± SEM of independent experiments each measured in triplicate wells (n = 2 – 8). **(G)** Ratio of absolute intracellular serine and glycine levels in SHMT1, MFT, SHMT2, and FPGS depleted HAP1 cells. Each dot represents an independent experiment in triplicate wells; mean ± SEM.

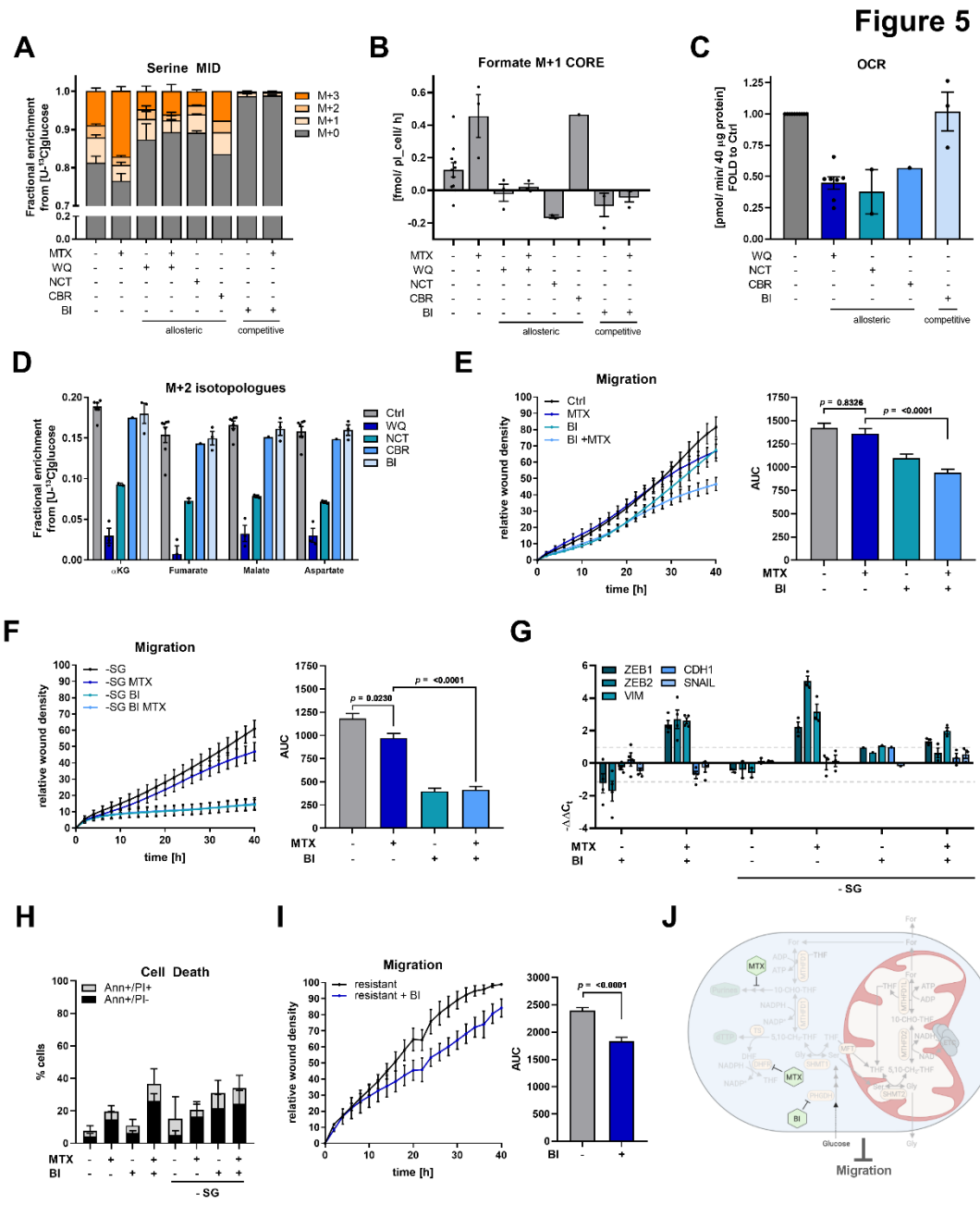

Figure 5: Targeting *de novo* serine synthesis decreases MTX-dependent cancer cell migration. (A) MID of intracellular serine upon [U-^{13}C]glucose tracer in MDA-MB468 cells in response to 24 h treatment with 10 µM WQ-2101, 10 µM NCT-502, 30 µM CBR-5884, 15 µM BI-4916, and 50 nM MTX as indicated; mean ± SEM of independent experiments each measured in triplicate wells (n = 1 – 9). **(B)** M+1 isotopologue of extracellular formate in MDA-MB468 cells using [U-^{13}C]glucose tracer upon treatment as in (A). Each dot indicates an independent experiment measured in triplicate wells; mean ± SEM. **(C)** Basal cellular respiration in response to 24 h 10 µM WQ-2101, 10 µM NCT-502, 30 µM CBR-5884, and 15 µM BI-4916 treatment was determined in MDA-MB468 cells as quantification of mitochondrial OCR. Graph shows fold OCR compared to untreated control. Each dot represents an individual experiment composed of six technical replicates; mean ± SEM. **(D)** M+2 isotopologues of indicated TCA-metabolites in MDA-MB468 cells using [U-^{13}C]glucose tracer upon treatment as in (B). Each dot indicates an independent experiment measured in triplicate wells; mean ± SEM. **(E)** Migration of MDA-MB468 cells in response to 50 nM MTX and 15 µM BI-4916 and respective AUC; mean ± SEM (n = 5); Brown-Forsythe and Welch one-way ANOVA with Dunnett's multiple comparisons test. **(F)** Migration of MDA-MB468 cells in response to 50 nM MTX, 15 µM BI-4916, and serine- and glycine starvation and respective AUC; mean ± SEM (n = 4); Brown-Forsythe and Welch one-way ANOVA with Dunnett's multiple comparisons test. **(G)** mRNA expression from the indicated target genes in MDA-MB468 cells in response to 72 h 50 nM MTX, 15 µM BI-4916, and serine- and glycine starvation as measured using real-time RT-qPCR. Each dot represents an independent experiment; mean ± SEM. **(H)** MDA-MB468 cells were treated for 48 h with 50 nM MTX and 15 µM BI-4916 under serine- and glycine starvation. Cell death induction was assessed by flow cytometry of AnnexinV-FITC/PI-stained cells; mean ± SD (n = 3). 2way ANOVA with Dunnett's multiple comparisons test. **(I)** Migration of MTX-resistant MDA-MB468 cells in response to 50 nM MTX and 15 µM BI-4916 and respective AUC; mean ± SEM (n = 4); Brown-Forsythe and Welch one-way ANOVA with Dunnett's multiple comparisons test. **(J)** Schematic depiction of the cytosolic and mitochondrial compartments of SOC and the pharmacologic intervention points of MTX and inhibitors of PHGDH.

Figure 6

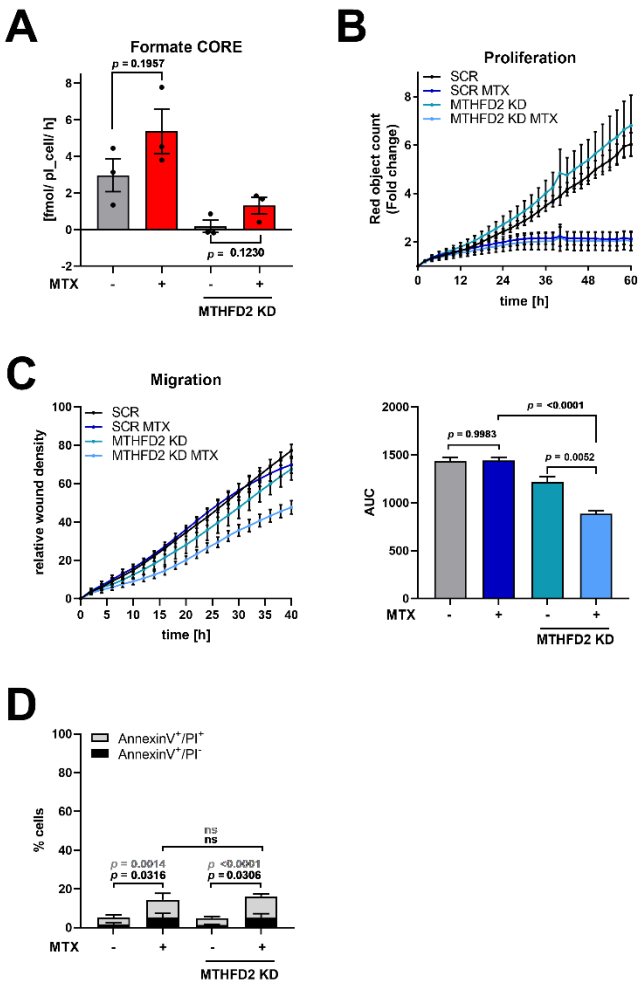

Figure 6: Targeting mitochondrial serine catabolism reduces MTX-dependent cell motility. (A) Absolute formate CORE rates of MDA-MB468 cells in response to MTHFD2 knockdown and treatment for 24 h with 50 nM MTX. Each dot indicates an independent experiment measured in triplicate wells; mean ± SEM; unpaired t-test with Welch's correction. **(B)** Proliferation of NucLight Rapid Red stained MDA-MB468 cells carrying a MTHFD2 knockdown in response to 50 nM MTX; mean ± SEM (n = 6). **(C)** Migration of MDA-MB468 cells in response to MTHFD2 knockdown and 50 nM MTX and respective AUC; mean ± SEM (n = 4); Brown-Forsythe and Welch one-way ANOVA with Dunnett's multiple comparisons test. **(D)** MDA-MB468 cells carrying a MTHFD2 knockdown were treated for 48 h with 50 nM MTX. Cell death induction was assessed by flow cytometry of AnnexinV-APC/PI-stained cells; mean ± SD (n = 4). 2way ANOVA with Dunnett's multiple comparisons test.

Figure 7

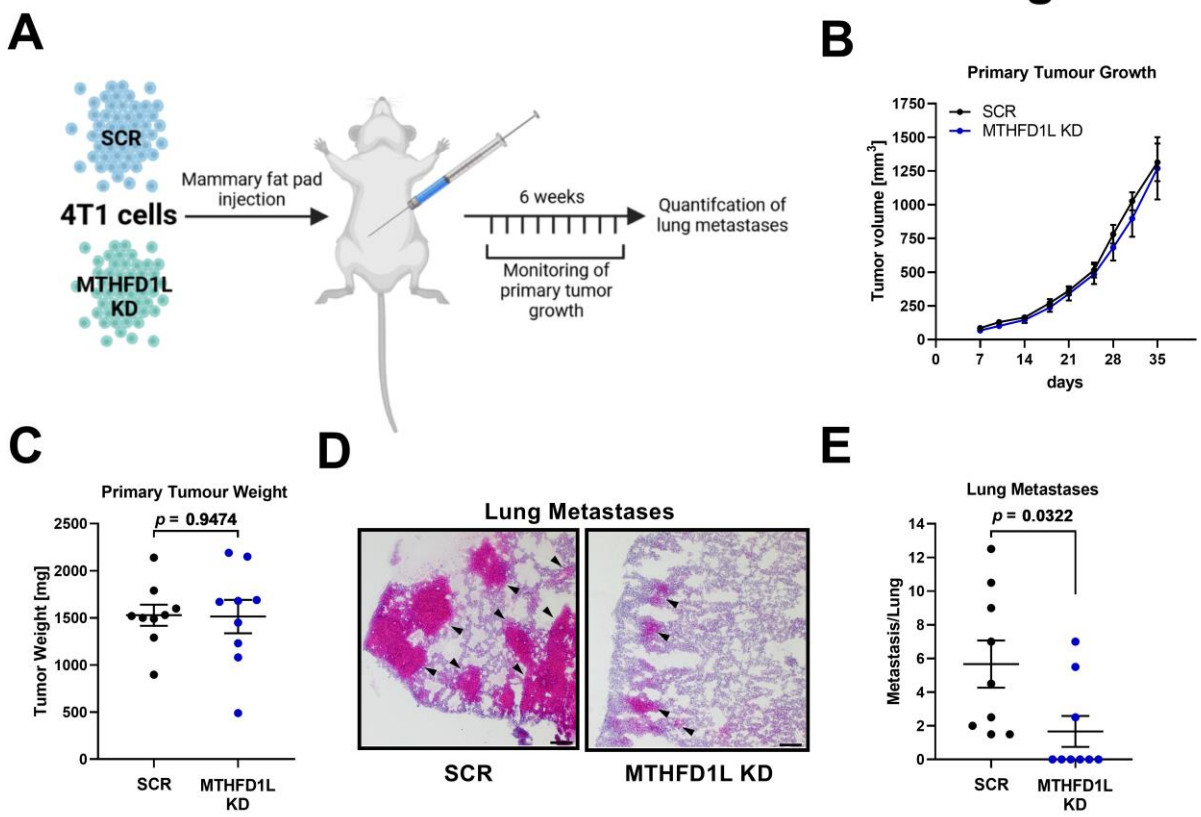

Figure 7: Genetic targeting of mitochondrial SOC reduces metastasis formation *in vivo*. (A) Experimental layout: immune competent female Balb/c mice were injected into mammary fat pads (1 injection/mouse in the left mammary fat pad) with 4T1 breast cancer cells transfected with non-targeting control (SCR, n=9) and 4T1 cells with knockdown of *Mthfd1l* (n=9). Primary tumor growth was monitored over time and lung metastases formation was evaluated at the end-point. **(B)** Primary tumor size was measured at the indicated time points and mean tumor volume was calculated. Data are presented as tumor volume ± SEM at each time point following injection with 4T1 SCR and *Mthfd1l* KD cells. **(C)** Primary tumor weight was measured at the end-point. Each dot indicates an independent animal; mean ± SEM; unpaired t-test with Welch's correction. **(D)** Lung tissue was stained with H&E stain. Representative pictures show microscopic lung metastasis in mice after orthotopic injection of 4T1 SCR and *Mthfd1l* KD cells. Arrows indicate metastatic nodules. Scale bar corresponds to 100 µm. **(E)** Macroscopic lung metastases were counted and number of metastases per lung is depicted. Each dot indicates an independent animal; mean ± SEM; unpaired t-test with Welch's correction.